MODELING AND ANALYSIS OF GEOTHERMAL ORGANIC RANKINE CYCLE TURBINES COUPLED WITH ASYNCHRONOUS GENERATORS AS A PRIMARY POWER SOURCE IN ISLANDED MICROGRIDS

By
Nathan Green, B.S.

A Thesis Submitted in Partial Fulfillment of the Requirements
for the Degree of
MASTER OF SCIENCE
in
Electrical Engineering

University of Alaska Fairbanks
May 2019

APPROVED:

Dr. Richard Wies, Committee Chair
Dr. Daisy Huang, Committee Member
Dr. Mariko Shirazi, Committee Member
Dr. Charlie Mayer, Chair
Electrical & Computer Engineering
Dr. William Schnabel, Dean
College of Engineering & Mines
Dr. Michael Castellini, Dean
Graduate School

Abstract

Local renewable resources, such as geothermal hot springs, are being explored as prime electric power and heat sources in remote permanently islanded microgrids, and in some cases these renewable resources have already been implemented. In these types of remote areas, diesel electric generation is typically the prime source of power, even in areas where alternative resources are readily available, despite the high fuel cost due to transportation. This thesis shows that geothermal hot springs, when locally available, can provide primary power for these remote microgrids with temperatures as low as 20 °C below the boiling point of water. The geothermal heat can be converted to electrical energy using an organic Rankine cycle turbine in combination with a self-excited induction generator. A steady-state energy balance model has been developed using MATLAB® and Simulink® for simulating greenfield and brownfield geothermal microgrids at Pilgrim Hot Springs, Alaska and Bergstaðir, Iceland, respectively, to demonstrate viability of this microgrid design. The results of the simulations have shown that modest loads can be primarily powered off of these low temperature geothermal organic Rankine cycles over long time scales. As expected, more power is available during colder months when sink temperatures are lower, thus increasing the temperature differential. More research is needed to examine system response over shorter time scale transients, which are beyond the scope of this work.

Acknowledgments

I would like to thank …

My friends & family for helping cultivate the person who I have become.

All the members of my committee, both past and present, for guiding me.

Everyone at ACEP for supporting me.

And Sarah for inspiring me.

Table of Contents

List of Figures

Page

List of Tables

List of Symbols

Acronyms

AC	Alternating current
ACEP	Alaska Center for Energy and Power
CSI	Current source inverter
DC	Direct current
DER	Distributed energy resource
DFIG	Doubly fed induction generator
ESS	Energy storage system
MPPT	Maximum power point tracking
NIST	National Institue of Standards and Technology
ORC	Organic Rankine cycle
PFM	Pulse frequency modulation
PMSG	Permanent magnet synchronous generator
PWM	Pulse width modulation
R245-fa	Working fluid $CF_3CH_2CHF_2$ (1,1,1,3,3- pentafluoropropane)
SCIG	Squirrel cage induction generator
SEIG	Self excited induction generator
VFD	Variable frequency drive
VSD	Variable speed drive
VSI	Voltage source inverter

Subscripts

atm	Atmospheric pressure
$bearing$	Induction machine friction due to bearings

c,i	Cool fluid inlet
c	Core
esr	Electronic series resistance
gen	Generator
gross	Gross output
h,i	Hot fluid inlet
hi	High pressure side of the cycle
init	Inital condition of the working fluid
inv	Inverter
i	Inlet
ll	Line to line
load	Load
loss	Device losses
low	Low pressure side of the cycle
max	Maximum
mech needed	Mechanical power needed
mech	Mechanical
min	Minimum
m	Magnetization
o	Outlet
ph	Phase
r	Ratio
r	Rotor
sink	Sink fluid

$_{source}$	Source fluid	
$_{synch}$	Synchronous	
$_{s}$	Stator	
$_{water}$	Water	
$_{wf}$	Working fluid	
$_{windage}$	Induction machine friction due to windage	
$_{x}$	Excitation	

Variables

$\dot{m}$	Mass flow rate	$\mathrm{kg\,s^{-1}}$
$\dot{Q}$	Themal heat flow rate	$\mathrm{kW_{th}}$
ϵ	Effectiveness of a heat exchanger.	
ω	Angular frequency	$\mathrm{rad\,s^{-1}}$
A	Heat transfer area of a heat exhcanger	$\mathrm{m^2}$
a	Ratio of electrical frequency to synchronous frequency	
b	Ratio of rotor speed to synchronous speed	
C	Heat capacity rate of a fluid	$\mathrm{J\,s^{-1}\,K^{-1}}$
c_p	Mass specific heat of a fluid at constant pressure	$\mathrm{J\,kg^{-1}\,K^{-1}}$
D	Duty cycle	
E	Internal induced voltage of rotating machine	V
f	Frequency	Hz
H	Enthalpy of a fluid	J
h	Mass specific enthalpy of a fluid	$\mathrm{J\,kg^{-1}}$
L	Inductance	H
n	Rotational velocity	rpm

NTU	Number of transfer units of a heat exchanger	$\mathrm{K\,s\,J^{-1}}$
P	Mechanical or active electrical power	kW
p	Aboluete fluid pressure	Pa
$poles$	Number of poles in electrical machine	
Q	Reactive electrical power	VAR
R	Resistance	Ω
S	Mass specific entropy of a fluid	$\mathrm{J\,kg^{-1}\,K^{-1}}$
s	Slip of induction machine	
T	Time of one period in a cycle	s
t_{on}	Time a switch is in the on state	s
U	Internal energy of a fluid	J
U	Overall heat transfer coffecicient of a heat exchanger	$\mathrm{J\,m^{-2}\,s^{-1}\,K^{-1}}$
V	Fluid volume	$\mathrm{m^3}$
V	Voltage	V
X	Reactance	Ω
Y	Admittance	℧
Z	Impedance	Ω

Chapter 1

Introduction

1.1 Problem Statement

Many communities in northern latitudes, such as the state of Alaska, are electrically isolated from the rest of the state, province, or country, effectively acting as remote permanently islanded microgrids. These communities typically use diesel generators to provide most of their electrical power. Power sources such as coal or natural gas are less expensive in larger grids, but these microgrids are too small to take advantage of such economies of scale. This makes it expensive to operate relative to the size of the communities. Furthermore, the remoteness of these communities significantly increases the cost to import fuel.

The goal of this thesis is to examine an affordable method to incorporate geothermal resources into microgrids without compromising stability and reliability. One method of reducing operating costs is to offset diesel fuel through the use of locally available renewable energy resources.[1] However, powering a microgrid with a significant portion of intermittent renewable resources can negatively impact grid stability unless appropriate control systems are included.

This thesis will describe the simulations and analyses conducted to accomplish this goal. Specifically, permanently islanded microgrids containing geothermal organic Rankine cycle (ORC) power generation will be simulated and analyzed for greenfield and brownfield site applications. In both cases the geothermal power will be converted from AC to DC then back to AC for distribution to the loads.

- One greenfield site will be examined with no existing permanent electrical infrastructure.
- One brownfield site will be examined where there is an existing grid connection but experiences regular outages.

---

[1] Sometimes called renewables, these sources of energy either will not be depleted or can be replenished in a reasonably short period of time. They include wind, solar, geothermal heat, biomass, and water flow.

1.2 Geothermal Site and ORC Development

The simulations of the case study sites will use temperature and flow rate data from actual sites located in remote high latitude areas with accessible geothermal hot spring resources. The greenfield and brownfield case studies will be based off of the Pilgrim Hot Springs in Alaska and Bergstaðir, Iceland, respectively. Both geothermal resources have been studied previously, though they have undergone different levels of development.

Pilgrim Hot Springs, lies about 60 miles north of Nome in western Alaska. Since the 1970s there has been interest in developing the hot springs in order to generate electricity. Several exploratory wells have been drilled and indicate potential for low temperature geothermal electrical generation [1]. Figure 1.1 shows a geothermal runoff stream and how much warmer the water is compared to the banks. The area is currently undeveloped,[2] therefore, this remote microgrid will be designed from the ground up. The land owners, Unataaq LLC, have expressed interest in developing the resource as a tourist attraction, for agriculture, as well as for electrical production. They are currently working with the Alaska Center for Energy and Power (ACEP), a research group at the University of Alaska Fairbanks, to fulfill these goals.

The greenfield system would be similar to the organic Rankine cycle generator used at Chena Hot Springs. Though near Fairbanks, Alaska, these hot springs are not connected to the larger grid, and primarily use diesel generators to produce electric power. In an effort to reduce fuel usage, the owner worked with United Technologies and Carrier Refrigeration to install two 200 kW ORC generators to supplement the diesel generation. At the time of construction, the system found at Chena Hot Springs made use of the lowest temperature geothermal resource for operating ORCs [2]. In addition to the ORCs, Chena uses the geothermal hot water to heat cabins and greenhouses, as well as for sitting pools.

---

[2] There are historic ruins of an old church and orphanage from the early 1900s, but those buildings are uninhabitable.

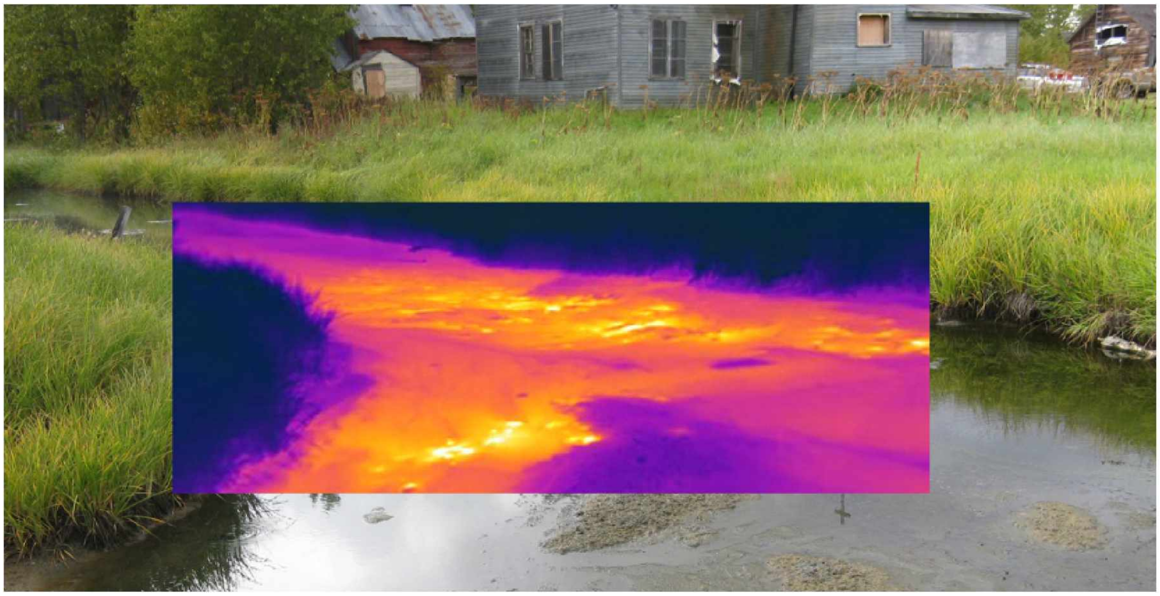

Figure 1.1. A FLIR thermal camera image of a Pilgrim Hot Springs geothermal runoff stream overlayed onto a photo. Credit: ACEP

Iceland has extensive experience utilizing their geothermal resources, but so far only high temperature areas are used for electricity production, while low temperature sites are used for district heating. One such system, and the brownfield case study for this work, heats the community of Bergstaðir, Iceland, a rural area in the inner part of the island east of Reykjavík. Figure 1.2 shows the discharge pipe and steaming effluent of the system. The pumps used to circulate the water are electrically driven by two 15 kW motors, but the electrical grid in rural Iceland is less reliable than the heating loop needs to be. Currently the community uses diesel generators to power the pumps during power outages, but they are interested in alternatives.

Figure 1.3 shows a simplified flow diagram of the model using an ORC as the power source. For the greenfield case, this represents standard operation of the hypothetical microgrid. For the brownfield case this represents only occasions when the microgrid becomes islanded from the larger grid and the ORC can power the load on its own. The components of the figure include an ORC system as a source,

Figure 1.2. District heating effluent at Bergstaðir, Iceland. Credit: George Roe.

a load, and an inverter to link the source output to the load. In the figure, the blue lines represent electrical connections, while green represents the flow of data and component parameters. The ORC block is composed of evaporating and condensing heat exchangers, an isentropic pump, an isentropic expander, and self-excited induction generator.

1.3 Microgrid Description

Microgrids are electrical systems composed of sources and loads within a well defined electrical boundary. Many microgrids are connected to a larger grid, but with the ability to become separated, or islanded, while still maintaining some or all of

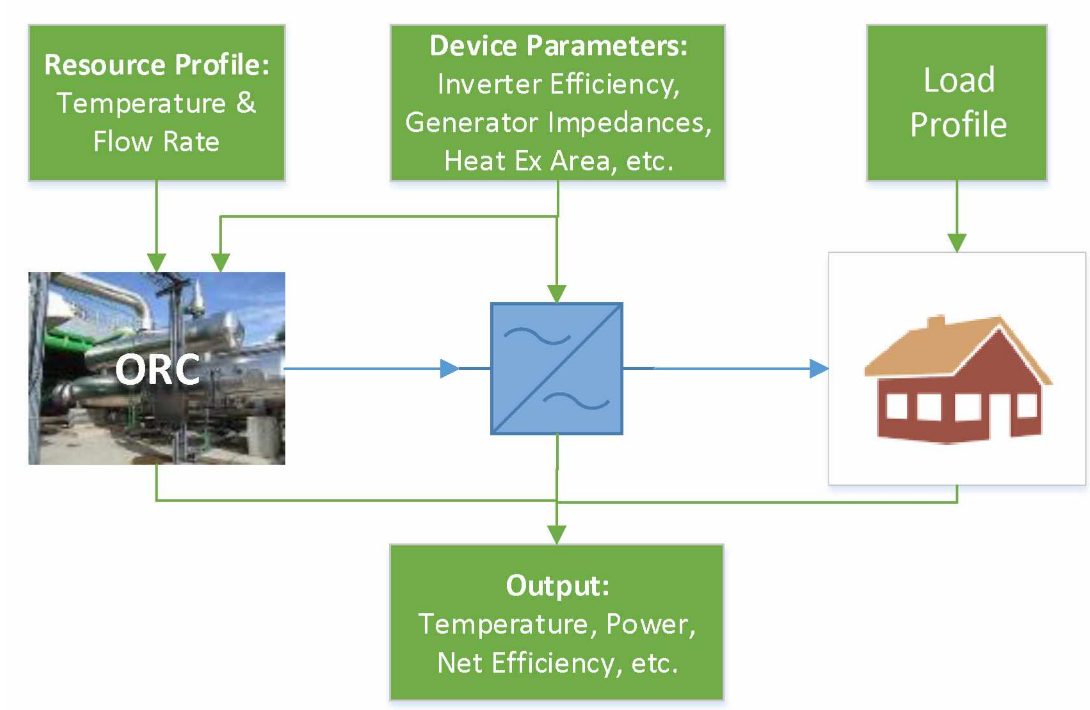

Figure 1.3. A simplified block diagram of power and data flows of the model. Blue arrows represent electrical power connections and flows similar to a one-line diagram. Green boxes and arrows represent data flow from one part of the model to another.

the loads. Others need to remain connected but still maintain a boundary. Some form of energy storage is often used for systems operating independently from the larger grid. This section will describe the key components and characteristics of a microgrid with emphasis on relevance to Alaska.

Approximately 70% of the population of Alaska is connected to a single grid called the Railbelt [3]. The Railbelt stretches over 600 miles from Homer on the Kenai Peninsula to the greater Fairbanks area in the interior and includes most communities on the road system. The remaining communities and villages are permanently islanded microgrids. Each has loads that need power, some power source, and some system of storing the energy or fuel.

A microgrid can operate using alternating current (AC), direct current (DC), or a hybridization of the two. The choice of whether to use AC[3] or DC depends on the demand of the loads, the available power sources and conversion devices, as well as the existing electrical infrastructure. The decision between AC and DC goes as far back as the 1880s when George Westinghouse and Thomas Edison were competing to supply America with electrical power. Ultimately Westinghouse and AC came out on top in part due to its relative ease of transforming to high voltage and low current which transmits more efficiently [4]. Furthermore, electric machinery that uses AC to generate rotating magnetic fields operates more efficiently than machines which use DC power and commutators. Like most of the world, Alaska uses AC networks and converts to DC as necessary at the device level.

While AC is still the standard for most power distribution and transmission, DC applications are seeing increased attention. DC interties are already used to connect large areas of the national power grid and to act as a buffer for frequency and voltage variations between each part of the system. DC microgrids also have the potential to improve stability with distributed, intermittent, and highly variable renewable generation, although much work is still needed. Integration of AC and DC infrastructure remains challenging for adaptation into existing systems, though low-cost solid-state power electronic converters increase the viability of greenfield DC microgrids.

1.3.1 Sources

Microgrid power is typically generated by distributed energy resources (DER). This can include renewable resources such as solar photovoltaics, wind turbine generators, hydrokinetics, biomass, and geothermal-based generators. Some non-renewable DERs include diesel generators and natural gas micro-turbines.

---

[3] Unless otherwise noted, AC will refer to three phases separated by a phase angle of 120° rather than a single phase.

Diesel generators use the combustion of diesel fuel to spin an alternator producing AC power. These generators are prolific in rural Alaska generally being used as the prime mover to regulate grid frequency and voltage. The communities generally purchase the fuel in bulk once or twice each year because of their remote locations. The fuel is then stored in tank farms. Due to the widespread use of diesel generators in Alaska, significant energy cost savings can be realized by reducing fuel consumption through efficiency improvements and use of renewable energy sources.

This thesis is focused on using geothermal generators, in particular, as a prime renewable energy source to displace the fuel consumption of diesel generation. Geothermal generators are heat engines, and operate similarly to those used in traditional coal and nuclear plants. Heat causes a working fluid to thermally expand and change phases, thus spinning a turbine to produce AC power. The primary difference is that geothermal systems get heat from the Earth as opposed to combustion or nuclear reactions. Geothermal generators can be divided into high heat and low heat categories. High heat geothermal systems work with temperatures well above the boiling point of water, which means water can be used as the working fluid. Low heat systems operate at temperatures near or below the boiling point of water, therefore, a refrigerant must be used as an alternative working fluid.

1.3.2 Loads

Well designed microgrids are sized and configured around expected loads. Loads require a supply of active as well as reactive power. Reactive power cannot do any net work, but is necessary to sustain magnetic or electric fields and maintain the frequency and voltage of the grid. Any work done by the field is due to active power. Active power, also called real power, is associated with resistive loads. While resistive loads consume active power and inductive loads consume reactive power, capacitive loads generate reactive power and are often used to reduce the reactive power demand from the main generation sources in a grid.

Regardless of the type of load, there must always be a power balance among sources, loads, power in and out of storage, and losses. If the total load increases above generation, either additional sources must be brought online or other loads must be shed. It costs money to bring more sources online, particularly fuel based sources, therefore, it is better to decrease the load if possible. Certain flexible loads can be designated as dispatchable. They require a certain amount of energy over a period of time but not continuously or on demand. These loads can be shut off automatically or forced to remain off during periods of high energy use. Additionally, if the power generated by intermittent renewable resources exceeds the power consumed by normal loads, dispatchable loads can be activated sooner than they otherwise would be. This can potentially maximize fuel displaced by the renewable resources. However, the dispatchable loads require additional infrastructure and controls in order to communicate with other grid components to know when to turn on and off.

1.3.3 Storage

Energy storage is beneficial to microgrid operation because it allows generation to be spread over time. Energy Storage Systems (ESS) can include batteries, flywheels, super-capacitors, pumped hydro, and more. These devices have different storage duration and discharge times making various storage technologies advantageous in different situations [5]. The discharge of bulk energy storage over the course of many hours allows for load leveling. Load peak shaving typically involves a discharge time from minutes to hours. Energy storage discharge over seconds and sub-seconds is generally done to improve power quality.

1.3.4 Conversion

Electronic conversion devices take a form of electrical power (AC or DC) and convert it into a different form. Power conversion devices typically use switching components such as diodes or transistors to control the output voltage and current waveforms.[4] Inductors and capacitors provide filtering as well as ensure continuous levels of the voltage and current. These elements provide a short term energy storage medium to allow transfer of energy from on form to another. Inverters convert DC power into sinusoidal AC power. Rectifiers convert AC to DC. DC-DC converters can step up or down the voltage level of a DC power source. Variable frequency drives (VFD)[5] modify the frequency of an AC source by rectifying the AC source and then inverting that output back to AC at the desired frequency. While transformers are not actually power electronic conversion devices the provide a similar function as DC-DC converters by stepping up or down the voltage level of an AC source by magnetic induction while maintaining frequency.

1.3.5 Control

A microgrid control system ties all the other components together. Control systems monitor and maintain the voltage and frequency of the grid while ensuring sufficient active and reactive power is supplied to the loads. The control schemes of power sources and converters can generally be divided into several categories: grid-forming, grid-following, grid-supporting, and grid-parallel [6, 7, 8].

Grid-forming units set the frequency and voltage levels of the microgrid. Grid-following units control the power[6] supplied to the grid based on external reference values from the loads. Grid-supporting units provide power based on voltage and frequency regulation. They assist the grid-forming unit with maintaining the voltage and frequency while also supplying power. Grid-parallel units also supply

---

[4] The major exceptions are transformers.

[5] Sometimes called Variable Speed Drives (VSD)

[6] Both active power and reactive power.

power to the grid, but it is based on reference values of a source. These units typically incorporate a maximum power point tracking (MPPT) algorithm in order to produce as much power as is available to serve the load. They are used with intermittent sources such as wind turbines and solar PV arrays.

Control over DER and electronic conversion devices can also be categorized by whether or not communication is used. Typically communication among converters can yield more precise power sharing and set points, but the necessary communication lines can introduce additional costs and points of failure [9]. Furthermore, control strategies that do not require communication are easier to expand and provide redundancy because coordination among controller units is less complex. Methods of communication based control include centralized, distributed, and master/slave control. Methods of non-communication based control include droop control as well as frequency-based signal injection.

1.3.5.1 Communication Based Control

Centralized control schemes make use of two-way communication where a central controller sets the priorities of local DER and load controllers during regular intervals. The priorities are determined from a predefined optimization algorithm and use inputs of power supply and demand from the local controllers, as well as market costs during the previous interval [10]. Distributed control schemes also use a centralized control unit to regulate the set points of the local control units, but simpler communications are used. The central control unit responds more slowly to disturbances than the local controllers, but helps ensure they share power evenly in steady state conditions [11].

In a master/slave relationship among different DER units, the master will operate in voltage control mode and the slave units in current control mode. Such a system may or may not include a central controller. In systems with a central controller, that controller sets the current references for the slaved units [12]. Otherwise, it is the master unit that sets the current references [13].

1.3.5.2 Non-Communication Based Control

The droop control method originated with the relationship between frequency and active power for synchronous machines due to rotating inertia. As load increases the machines in the system will slow and the system frequency will droop or decrease. It has since been adapted into power conversion control schemes as well despite the lack of physical inertia and often referred to as synthetic or virtual inertia. It is mathematically derived from the equation describing active power flow, P, through an impedance $R + jX$ from point 1 to point 2, as seen in Figure 1.4, where

$$P = \frac{V_1}{R^2 + X^2}\left(R\left(V_1 - V_2 \cos \delta_{12}\right) + XV_2 \sin \delta_{12}\right). \tag{1.1}$$

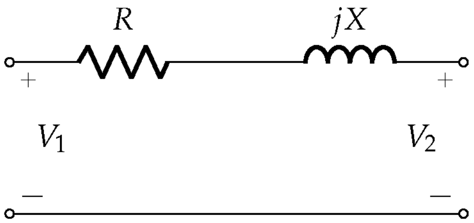

Figure 1.4. Circuit diagram demonstrating power flow from V_1 to V_2 across impedance $R + jX$.

Assuming a small phase angle δ_{12} between the points as well as negligible resistance R, the equation can be reduced to

$$P = \frac{V_1 V_2}{X}\delta_{12}. \tag{1.2}$$

In practice, frequency is used rather than angle because individual units cannot know the phase of other units without communication. For power and frequency deviation from predefined references the droop equation becomes

$$f = f_{\text{ref}} + K_P\left(P - P_{\text{ref}}\right) \tag{1.3}$$

where K_P is a negative proportionality constant.

Similarly a droop relationship between reactive power flow and relative voltage levels can be shown, where

$$Q = \frac{V_1}{R^2 + X^2} \big(- RV_2 \sin \delta_{12} + X \left(V_1 - V_2 \cos \delta_{12} \right) \big) \tag{1.4}$$

can, for small angles, be approximated as

$$Q = \frac{V_1}{X} \left(V_1 - V_2 \right), \tag{1.5}$$

and the droop relationship is

$$V = V_{\text{ref}} + K_Q \left(Q - Q_{\text{ref}} \right) \tag{1.6}$$

where K_Q is a negative proportionality constant.

It should be noted, however, that the droop equations are only valid under certain conditions. If the angle/frequency deviations are too large then the small angle approximations will break down. Additionally, the relative magnitude of the resistive and reactive impedance components affect system dynamics. If the frequency changes are too large then X can no longer be considered constant. This means the P/f and Q/V relationships cannot be approximated as linear. Additionally, the line resistance in most low voltage systems is not so small as to be negligible. In fact in situations where the line reactance is negligible compared to the resistance, linear approximations can be made between active power and voltage as well as reactive power and frequency [14].

1.4 AC vs DC Microgrids

AC microgrids and DC microgrids are both technically feasible, but the selection of which is optimal for a given application heavily depends on the types of loads and power sources used. Furthermore, the choice is not necessarily a binary decision. AC/DC hybrid systems can provide the benefits of each architecture, but at greater cost. This section will compare and contrast the different architectures based on efficiency, stability, and economic considerations.

1.4.1 Efficiency

In each conversion step there is some power loss due to inefficiencies. Sequential conversions can add up to a significant loss. Distributing AC and DC power to their respective loads separately can eliminate many conversion steps, but it is unrealistic to completely remove all steps. Table 1.1 shows that, at rated values, typical losses among different power converters are not symmetric. Transformers are the most efficient, followed by inverters and DC-DC converters. Rectifiers incur the most loss. When operated below rated values all conversion devices experience drops in efficiency.

Table 1.1. Efficiencies of typical transformers and power conversion devices.

		From	
		AC	DC
To	AC	98% [15]	97% [15]
	DC	90% [16]	95% [15]

Additionally, transmission and distribution power losses are not identical for AC and DC systems. In normal conditions, three phase AC systems undergo loss in three lines, one for each phase, while DC systems only experience power loss in two, the high voltage side and low voltage side. For AC and DC systems experiencing equal distribution losses across the same lines, the ratio of RMS AC current to DC current is given as [15]

$$\frac{I_{AC}}{I_{DC}} = \sqrt{\frac{2}{3}} \approx 0.82. \tag{1.7}$$

If in addition to equal power distribution losses the systems also deliver equal power to their respective loads, then the AC voltage to DC voltage relationship is

$$\frac{V_{AC}}{V_{DC}} = \frac{1}{\sqrt{6}\cos\theta} \approx \frac{0.41}{\cos\theta}, \tag{1.8}$$

where θ is the phase angle between V_{AC} and I_{AC}. In other words, to deliver power to equivalent loads and experience equal power losses, DC current and voltage must be greater than AC RMS values. However, if the two systems deliver the same power and current, then the DC system will experience lower power losses due to distribution lines.

1.4.2 Stability

Electric machinery and power electronic conversion devices introduce undesired harmonics into AC grids due to non-linear loading and switching effects [17]. Harmonic distortion can cause power losses as well as reduce voltage and frequency stability. Because harmonics are, by definition, based off of a fundamental frequency, the harmonics alone are not an issue in DC segments of a microgrid system. DC systems can experience stability issues caused by non-linear loads such as spikes in current and voltage.

Another important factor in grid stability is how quickly and safely the system can clear an electrical fault. The sinusoidal oscillation of AC systems means there is a periodic zero crossing 60 times each second.[7] This means faults can be cleared more quickly in AC systems than in DC systems. However, AC systems typically experience larger transient spikes during fault events when compared to DC systems at similar power and voltage levels [18].

1.4.3 Economics

Most existing electrical infrastructure is built around AC grids rather than DC grids. Furthermore off the shelf electrical appliances generally assume AC power is available and will rectify to DC if needed. These factors indicate the installation of an AC distribution system is more economical. However, three phase AC systems require three lines, one for each phase, and sometimes a forth neutral line,

---

[7] For regions that operate on 60 Hz.

while bipolar DC systems only require two lines, and sometimes a third neutral line.[8] However, the economic benefit of fewer electrical lines is much more significant for long distance transmission than for distribution to nearby loads.

One benefit of DC microgrids over AC is the necessity to control only voltage level rather than voltage and frequency. A simplified control scheme can reduce the cost. Additionally, combining power sources into a DC bus before distribution avoids the necessity of synchronization [19].

1.5 Thesis Organization

With the background information on microgrids addressed in Chapter 1 above, the remainder of the thesis is organized as follows. Chapter 2 delves deeper into background of power conversion. This includes the conversion of heat to electricity with a focus on low-temperature sources, as well as electrical power conversion focusing on the pros and cons of different topologies. Chapter 3 details development of the geothermal ORC prime power model. Chapter 4 analyzes the model validations as well as simulation results of the greenfield and brownfield scenarios. Chapter 5 concludes the thesis and describes future work to be conducted on the topic.

---

[8] Although work has been done on Single Line Ground Return systems which only require one line.

Chapter 2

Energy Conversion

Energy and power take many different forms, from the initial sources to the end uses. Necessarily, methods have been developed to convert energy or power from one form to another. The first method addressed in this chapter is the conversion process of thermal to mechanical to electrical energy found in heat engines and generators. This thesis is focused on geothermal heat; however, heat engines can be used with a number of different sources including the burning of a fuel such as biomass or coal, or even as waste heat from an independent process. The conversion between different forms of thermal energy and electrical power will also be discussed including electrical generators and power electronic converters that are used to form a grid in ORC prime power systems.

2.1 Thermal Energy

Thermal energy, or heat, can originate from many different sources including combustion of a fuel, radioactive decay, or absorption of light from the sun. Heat can be used directly to warm a building, but it is also a critical step in most traditional methods of generating electrical power.

2.1.1 Enthalpy

Enthalpy describes the energy of a system available to be converted to work. It is related to the temperature of the geothermal resource, but also dependent on the pressure and volume. Temperature is usually the primary metric of a resource, but even a high temperature source is useless without sufficient volume flow. Quantitatively enthalpy is expressed as [20]

$$H = U + pV \tag{2.1}$$

where U is the internal energy, which is function of temperature, p is the pressure of the system, and V is the volume. Generally it is more convenient to use the change in enthalpy rather than absolute values. After a system undergoes some thermodynamic process, the system will always have some remaining internal energy, pressure, and volume. Therefore, a change in enthalpy better describes the energy extracted from (or absorbed by) the system. Additionally, the enthalpy of a system is often normalized to its mass for comparison to other sized systems, and the mass specific enthalpy, h, is used instead.

2.1.2 Geothermal Cycles

Geothermal systems can be classified as high-, medium-, or low-enthalpy[1]. Although there is no formal delineation, high-enthalpy sources generally have temperatures greater than about 150 °C (302 °F) and low-enthalpy sources have temperatures lower than 100 °C (212 °F) [21]. Depending on the amount of extractable energy of the resource, different geothermal processes or cycles can be used to extract the maximum amount of energy from the resource.

2.1.2.1 Dry Steam

This high-enthalpy processes extracts hot steam from the earth. The steam is sent directly through a turbine then condensed into liquid water and injected back underground.

2.1.2.2 Flash Steam

In the flash steam process high pressure hot water is extracted then, allowed to boil becoming steam and low pressure hot water. The steam is sent through a turbine then condensed, recombined with water, and injected back underground.

---

[1] While the technical definitions differ, the terms enthalpy, heat, and temperature are often used interchangeably when qualitatively describing geothermal sources.

2.1.2.3 Binary Cycle

As the name implies, binary cycles involve two loops: a heat source loop and working fluid loop. Heat is collected in the heat source loop and transferred to the working loop through a heat exchanger. The working fluid then undergoes the vaporization process to spin a turbine or other type of expander. The expander is connected to a generator which converts the rotational mechanical energy into electrical energy. After some of the heat is converted, the working fluid passes through a condenser where it is cooled further. Sometimes the cooling process involves drawing in air at ambient temperature, but it can also involve a third loop dedicated to dissipating the unconverted heat. The fluids within each of the cycles must be moved using pumps. The pumps themselves need to be powered and are a parasitic load to the system.

Binary cycles are not limited to low or medium enthalpy heat sources. The most common binary cycle is the Rankine cycle. A diagram of the process can be seen in Figure 2.1. In an ideal Rankine cycle heat is added to the working fluid under high pressure to change its phase from liquid to gas. The fluid expands isentropically[2] which rotates the generator shaft, causing the fluid's temperature and pressure to drop. Additional heat is then expelled from the fluid as it condenses on the constant low pressure side of the system. Finally the fluid is isentropically pumped back to the high pressure side of the system and the process begins again.

For geothermal sources, high enthalpy systems can generally be implemented directly with a single loop using flash or dry steam processes. However, for lower enthalpy systems, water cannot be used as a working fluid because the temperatures are not high enough to vaporize it. In these cases an organic Rankine cycle, which uses an organic working fluid such as a refrigerant instead of water, can be employed. Working fluids are typically selected for relatively low vaporization temperatures, but the thermodynamic states of the heat source must also be considered. The selection of the size and type of expander and pumps are discussed

---

[2] In thermodynamics, isentropic processes do not have a net change in entropy.

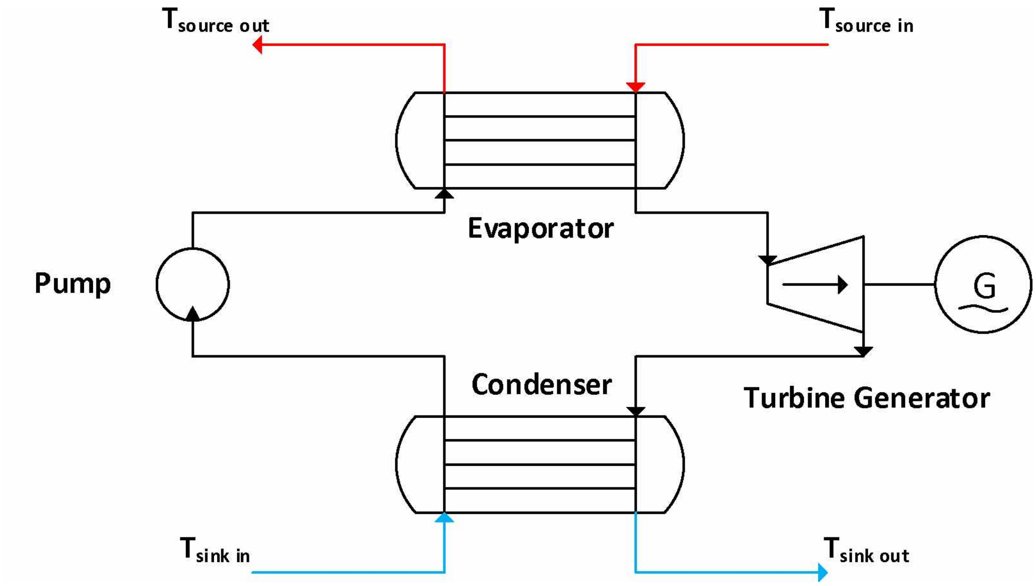

Figure 2.1. Diagram of a Rankine cycle system.

in Kreider [22]. For low speed applications, large diameter piston expanders may be most appropriate, where as smaller diameter axial turbines operate at faster speeds.

2.2 Electrical Generators

Electrical generators are spinning machines which convert the mechanical power rotating a shaft to electrical power. Fundamentally, they operate on the principles of Maxwell's and Faraday's laws which broadly state that a moving magnetic field produces an electric field and vice versa. The primary difference among generator types is how that magnetic field is produced.

2.2.1 Synchronous Generators

The magnetic field in synchronous generators is formed by external sources. The name derives from the fact that electric frequency directly synchronizes with the physical rotation of the machine.[3] They are also capable of supplying reactive power because the internal magnetic field is not self induced.

In traditional synchronous machines an electro-magnet is used to generate the field by running a DC current through the rotational, or rotor, windings. The spinning DC electric field produces a magnetic field, which in turn makes an electric field in the stationary, or stator, windings. By varying the DC current applied to the rotor, the user can control the voltage generated by the machine. The current sets the magnetic flux which in turn controls the voltage [23]. As discussed in subsection 1.3.5.2, droop control takes advantage of the relationship between voltage and reactive power to ensure they are appropriately balanced.

In permanent magnet synchronous generators (PMSG) bar magnets are used to form the magnetic field of the rotor. A benefit of using permanent magnets over electro-magnets is the lack of slip rings or brushes used to apply the DC current to the rotor winding. These components can introduce a source of friction and wear down over time. However, since permanent magnetic fields are fixed at the time of construction, the user cannot control the voltage of the machine without full power electronic conversion between the generator and the grid.

2.2.2 Asynchronous Generators

Asynchronous (induction) machines generate their internal magnetic fields by self-induction rather than from an external source. Since induction machines do not rely on an additional source to operate, induction machines generally have simpler designs and are less costly than synchronous machines. However, that also

---

[3] Certain wiring configurations add additional electromagnetic poles to machine which causes the mechanical speed to be slower than the electrical speed by a factor of the integer number of poles.

means they need to consume reactive power from the grid in order to maintain their magnetic field. This field relies on the relative difference in frequency between the stator, f_s, and rotor, f_r, fields. This relative difference in frequency is represented by the machine's slip, [23]

$$s = \frac{f_s - f_r}{f_s}. \tag{2.2}$$

The stator frequency is equal to the grid frequency at the output terminal, while the rotor frequency is determined by the rotor's speed in rpm, n_r, and number of poles, where

$$f_r = \frac{n_r \times poles}{120}. \tag{2.3}$$

The number of poles is based off the number of coil windings per phase and established at construction. When the machine's slip is positive, the field frequency in the stator is greater than in the rotor, and the machine operates as a motor. A negative slip means the rotor is spinning faster than the frequency of the stator and the machine is acting as a generator.

Some work has been done on self-excited induction generators (SEIG) [24, 25]. Instead of solely consuming reactive power from the grid, induction generators use a bank of capacitors connected at their terminals to supply the necessary reactive power in order to maintain the magnetic field in the rotor. However, a significant drawback to these devices is the lack of control over frequency and voltage [26]. SEIGs require some form of power electronic conversion at the output terminals to regulate the grid side frequency and voltage. This can be achieved with full power electronic conversion, similar to PMSGs, where the generator output is entirely rectified and inverted to synchronize with the grid. Alternatively, two sets of windings can be used around the rotor instead of one, in what is called a doubly fed induction generator (DFIG). The primary set form the stator, which connects directly with the grid[4] and is used to deliver power. The auxiliary set of windings are connected to the grid through a power electronic converter. This converter

---

[4] Via a transformer.

can be used to control the rotor current to ensure consistent frequency and voltage despite variable rotational speeds [27, 28].

2.3 Power Electronic Conversion

As described previously, power electronic conversion takes electric power from either an AC or DC form and converts it to a different form or level. This is generally done by switching the path of the input current to form the desired output using solid-state semiconductor devices. Control over the switching is critical for these conversion devices. Pulse Width Modulation (PWM) and Pulse Frequency Modulation (PFM) are two alternate methods of controlling switching states of the semiconductor devices. Both methods vary the duty cycle, D, of the control signal of the device in order to change the on/off state. The duty cycle is the fractional time a switch is on, t_{on}, relative to one period of the control signal, T, or

$$D = \frac{t_{on}}{T}. \tag{2.4}$$

For PWM the switching frequency is held constant while the duration of the pulse is varied to control the output. In PFM, the duration of each pulse is fixed while time between pulses, and therefore, the frequency varies.

2.3.1 DC-DC

DC-DC power conversion devices can generally be divided up into three simple designs: buck to step voltage down, boost to step voltage up, and buck-boost to step voltage down or up depending on the source voltage. There are additional DC-DC converter topologies which use the same concepts in these designs, but are modified to create different characteristics [29].

In a simple buck converter, seen in Figure 2.2, timed switching sets the average output voltage to a value smaller than the input voltage, or

$$V_{out} = DV_{in}. \tag{2.5}$$

The inductor ensures a continuous current at the output and the capacitor provides an output voltage with only modest ripple.

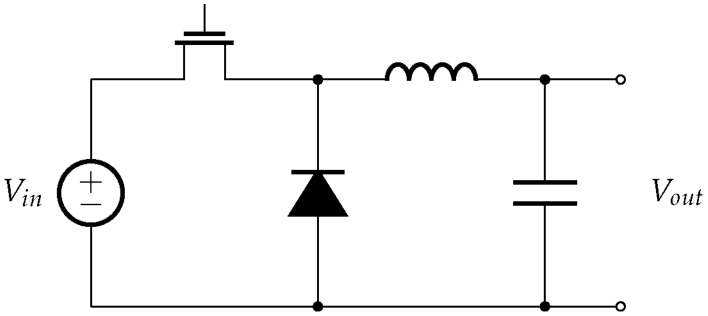

Figure 2.2. Simplified diagram of a buck converter.

In a simple boost converter, seen in Figure 2.3, timed switching also sets the average output voltage to the desired level, but with the relationship

$$V_{out} = \frac{V_{in}}{1 - D}. \tag{2.6}$$

However, the placement of the components leads to an increasing current through the inductor while the switch is closed. When the switch is open, the relatively high current flow through the diode results in a larger average output voltage than seen at the input. As in the buck converter, the capacitor provides an output voltage with modest ripple.

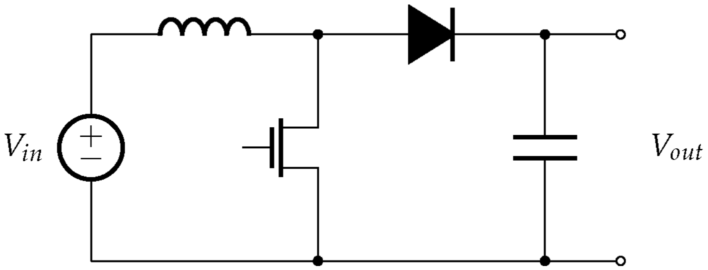

Figure 2.3. Simplified diagram of a boost converter.

These two topologies can be combined to form a buck-boost converter, seen in Figure 2.4 which has an input/output voltage relationship of

$$V_{out} = V_{in}\frac{D}{1-D}. \tag{2.7}$$

This configuration allows the output voltage to be either greater than the input voltage for $D > 0.5$ or less than the input voltage for $D < 0.5$. It must be noted that while this orientation gives a greater voltage range at the output, the output voltage has a negative polarity. With appropriate electrical isolation, the polarity should not impact the operation of the buck-boost converter. However, using a common ground between the input and output will cause the circuit to fail because the high side of the output voltage is necessarily at the same potential as the low side of the input voltage.

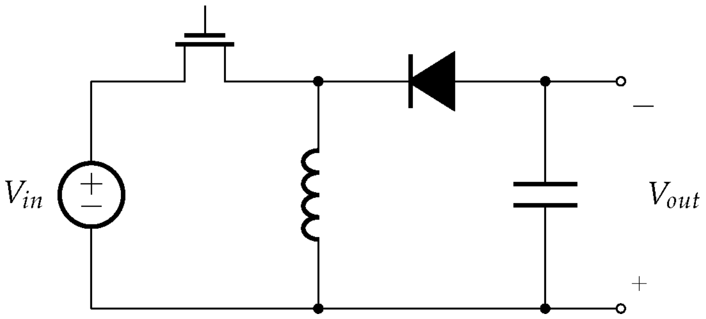

Figure 2.4. Simplified diagram of a buck-boost converter.

2.3.2 Rectifier and Inverter

Simple rectifiers use a combination of diodes to convert an AC voltage to DC. Figure 2.5 shows a simple example of a three phase rectifier. The diodes allow a path such that the DC current always flows in the same direction regardless of AC polarity. More advanced designs will use active switching devices and a control scheme to provide the same function. Though more complicated to implement, the user has more direct control over the output as well as how the load appears to the input.

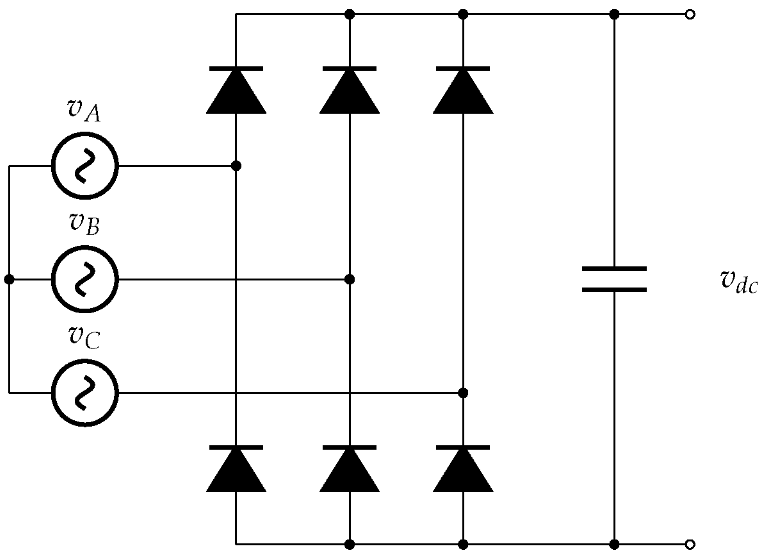

Figure 2.5. Simplified diagram of a three phase full-bridge rectifier.

Inverters function as rectifiers in reverse. A DC source is switched on and off such that it alternates periodically. The three phase inverter diagram, seen in Figure 2.6, is similar to the rectifier diagram, except the inverter must use active switching. In fact many inverters are designed to be reversible. The device can control the flow of active and reactive power in inverter mode or rectifier mode. The inductors and capacitors seen in the figure provide filtering, as with the single phase converters described previously.

Depending on how the inverter is expected to interact with other components on the grid, different control schemes may be needed to shape the output signal appropriately. When operating in a grid-forming mode, the inverter must be capable of regulating the frequency and voltage and is called a voltage source inverter (VSI) [7]. When an inverter is operating in grid-following mode, it uses the grid to set its output frequency and voltage and supplies power based on active and reactive power setpoints. Grid-following inverters are also called current source inverters (CSI). Grid-supporting units usually assist the grid-forming source or inverter with frequency and voltage regulation often using droop or similar methods

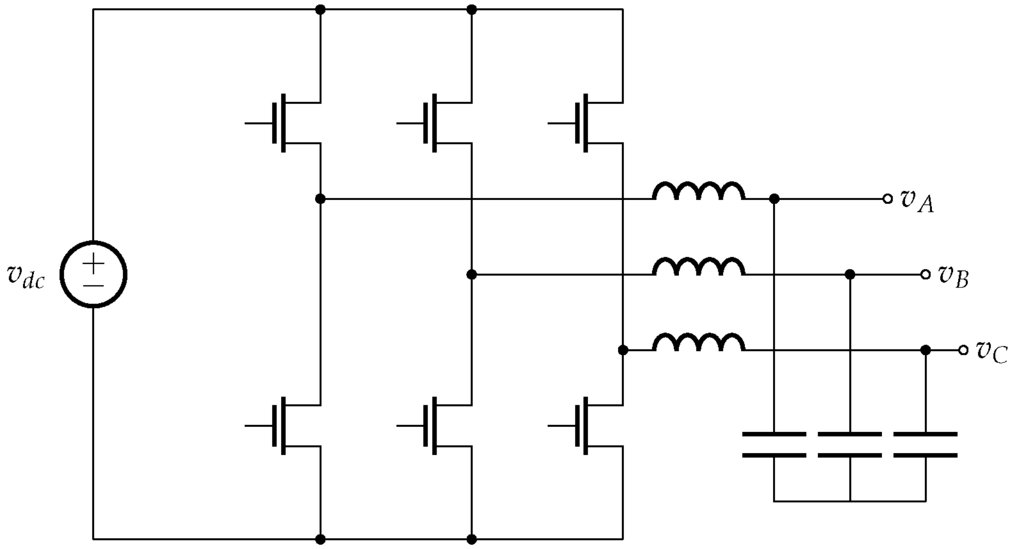

Figure 2.6. Simplified diagram of a three phase inverter.

of control as discussed in subsection 1.3.5.2. Lastly, grid-parallel inverters supply power based off of references at the input instead of the grid, and are often used with wind turbines and solar PV arrays to provide the maximum power possible [30].

2.3.3 AC-DC-AC

In certain situations, full power electronic conversion is necessary, where an AC source is rectified to DC, then inverted back to AC at the output. This is done when the power source is generating unregulated AC, such as with SEIGs and PMSGs, but the grid or load requires regulated AC [31, 32]. In other instances, either end of the converter is regulated independently, so a DC link is required to exchange power [33]. For example, the contiguous United States has three different grids whose relative frequencies may vary. DC interties between each one allows for the transfer of power without needing to synchronize them together.

2.4 Energy Conversion Model

Before simulating the prime power ORC system, it is critical to understand how different forms of power are converted from one to another in order to accurately simulate the overall process. To achieve this a thermodynamic model, a generator model, and a power electronic converter model were developed in order to mathematically describe converting heat to mechanical power, converting mechanical power to electrical power, and converting between different forms of electrical power, respectively. Additionally, commercial ORC manufacturers and their systems were investigated to better understand how they have applied the energy conversion methods described above. A list of these systems, the working fluids used, the mechanical drives, the approximate maximum rotational speeds, the generator types, and the rated output powers can be seen in Appendix A. This information helped better inform the energy balance model and as well as the simulations.

Chapter 3

Prime Power ORC System Model

The model attempts to recreate a microgrid which uses an ORC fed by geothermal resources as a primary power source in order to form a grid with a self-excited induction generator using full power electronic conversion. Figure 3.1 shows the ORC prime power system model flow diagram with all the variable inputs on the left and outputs on the right. The internal blocks include the ORC, the pump drive motor, the SEIG, and the full power electronic grid-forming inverter. The ORC block, itself, is composed of evaporating and condensing heat exchangers, as well as a pump and expander, both of which are assumed to be non-ideal isentropic processes.

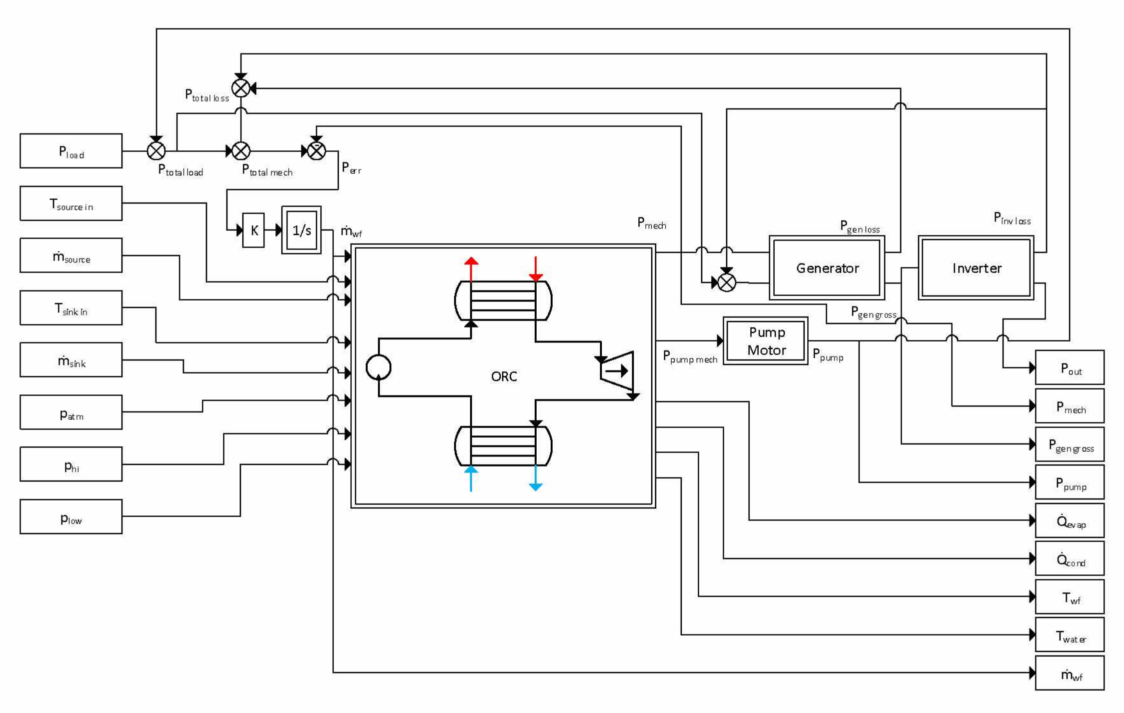

Figure 3.1. Organic Rankine cycle prime power system model diagram documenting data flows of the model. Boxes on the left side represent variable inputs, and those on the right indicate variable outputs.

3.1 Organic Rankine Cycle

The ORC block, seen in Figure 3.2, links the thermal, mechanical, and electrical components of the model. The thermal properties of the source, sink, and working fluids were obtained from a MATLAB® wrapper of the CoolProp© library. Thermal conditions of source, sink, and working fluids are input to the Rankine cycle portion of the model which returns a mechanical power.

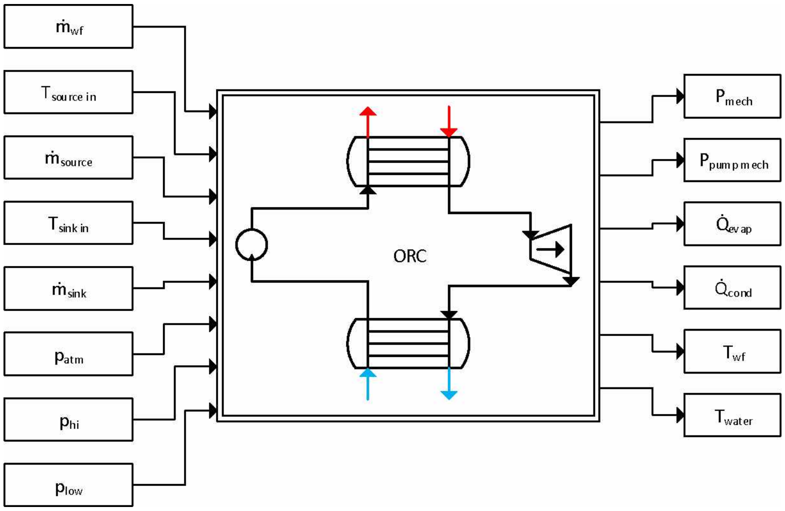

Figure 3.2. Organic Rankine cycle model diagram combining the pump, expander, and evaporating and condensing heat exchangers.

CoolProp© is an open source C++ library which contains thermophysical properties of over 110 fluids including the working fluids used in refrigeration processes [34]. It makes use of Helmholtz energy-explicit equations of state to derive its values, but can also incorporate the REFPROP library developed by the National Institute of Standards and Technology (NIST). Although originally written for C++, wrappers have been developed for many other common programming languages and analytical software including, but not limited to, MATLAB®, Python, Java, R, NI Lab View™, and Excel. Due to its wide availability and open source licensing, it has seen much use in the analysis of ORCs [35, 36], refrigeration units [37], and other applications [38, 39].

In order to use CoolProp©, first a handle is initialized for each of the source, sink, and working fluids. The handle is passed as a static parameter to any of the functions that require any thermophysical calculations. The function uses the handle during any calls of the CoolProp© library.

The variable inputs used for the ORC block include the mass flow rates for the source, $\dot{m}_{source}$, sink, $\dot{m}_{sink}$, and working fluids, $\dot{m}_{wf}$ ($\mathrm{kg\,s^{-1}}$), the inlet temperature of the source, $T_{source\ in}$, and sink, $T_{sink\ in}$ (K), the absolute pressures for the high side, p_{hi}, and low side of the cycle, p_{low}, as well as the pressures of source, $p_{source\ in}$, and sink fluid inlets, $p_{sink\ in}$ (Pa). In these simulations, $p_{source\ in}$ and $p_{sink\ in}$ are both assumed to be at atmospheric pressure, p_{atm}, though that is not a necessary condition. Fixed input parameters include the initial mass specific enthalpy of the working fluid feeding into the evaporator, h_{init} ($\mathrm{J\,kg^{-1}}$), as well as several values described in subsection 3.1.1 and subsection 3.1.2.

Before the inputs are fed into the sub-blocks, the fluid temperature and pressure combinations are converted to mass specific enthalpy values using CoolProp©. Similarly, mass specific enthalpy and pressure combinations are converted to temperatures before being output.

The output variables from the ORC block include the mechanical power produced by the expander, P_{mech} and consumed by the pump, $P_{mech\ pump}$ (W), the heat flow rates of the evaporator, $\dot{Q}_{evap}$, and condenser, $\dot{Q}_{cond}$ ($\mathrm{W_{th}}$), and the temperatures of the water, T_{water}, and working fluid, T_{wf} (K), at various points in the cycle. Specifically, T_{water} is composed of the inlet and outlet temperatures of the source and sink fluids, while T_{wf} contains temperatures at the inlets and outlets of the pump and expander and assumes there is no temperature drop through the lines to and from the heat exchangers.

3.1.1 Evaporator and Condenser

The evaporator and the condenser are both represented using a heat exchanger script. A block diagram of the function can be seen in Figure 3.3. The function takes as inputs variables characterizing hot and cool fluids, specifically the inlet mass specific enthalpies, $h_{h,i}$ and $h_{c,i}$ ($\mathrm{J\,kg^{-1}}$), mass flow rates, $\dot{m}_{h,i}$ and $\dot{m}_{c,i}$ ($\mathrm{kg\,s^{-1}}$), and inlet pressures, $p_{h,i}$ and $p_{c,i}$ (Pa). Additional static inputs include CoolProp© fluid handles, as well as parameters characterizing the exchanger itself such as the overall heat transfer coefficient, U ($\mathrm{W\,K^{-1}\,m^{-2}}$), the heat transfer area, A ($\mathrm{m^2}$), and a string describing the heat exchanger type (e.g. counter or parallel flow). The function output is made up of the heat flow rate, $\dot{Q}$ ($\mathrm{W_{th}}$), and the mass specific enthalpies at the outlets, $h_{h,o}$ and $h_{c,o}$ ($\mathrm{J\,kg^{-1}}$).

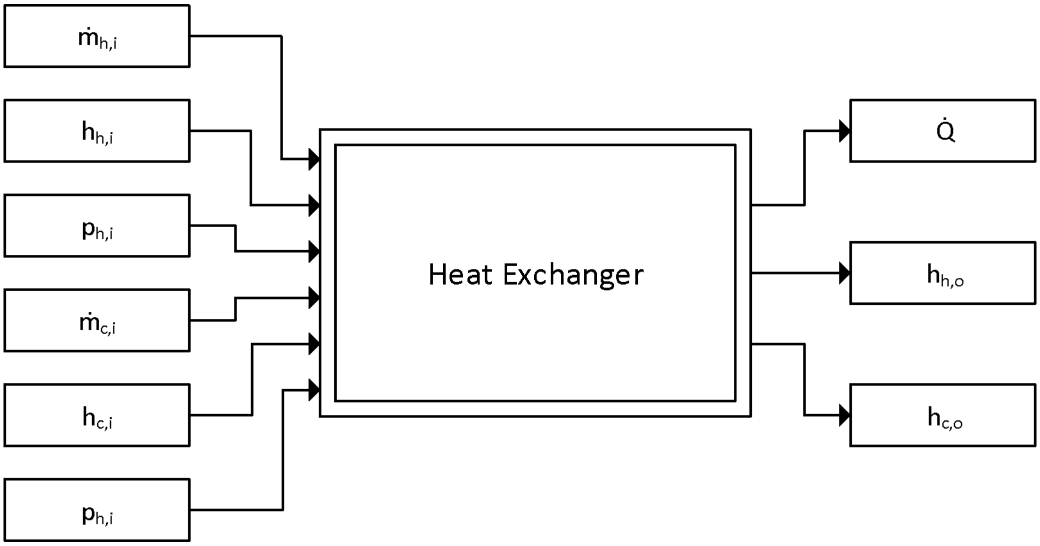

Figure 3.3. Heat exchanger model diagram showing variable inputs on the left and outputs on the right.

In order to calculate the desired values, the Number of Transfer Units (NTU) method is used. Described in The Fundamentals of Heat and Mass Transfer [40], this process calculates the output heat flow, $\dot{Q}$, relative to a theoretical maximum heat flow, $\dot{Q}_{max}$. This potential heat flow would be realized using an infinitely long counter flow geometry and is calculated as

$$\dot{Q}_{max} = C_{min}\left(T_{h,i} - T_{c,i}\right) \tag{3.1}$$

where C_{min} is the smaller heat capacity rate of the hot and cool fluids and $T_{h,i}$ and $T_{c,i}$ are the inlet temperatures of hot and cool fluids, respectively. The heat capacity rate is the product of mass flow rate, $\dot{m}$, and the mass specific heat at constant pressure, c_p, or

$$C = \dot{m} \cdot c_p. \tag{3.2}$$

The heat flow rates of the hot and cool fluids are related by the effectiveness, ϵ, which is defined as

$$\epsilon \equiv \frac{\dot{Q}}{\dot{Q}_{max}}. \tag{3.3}$$

Numerically, the value of ϵ is a function of the ratio of the fluids' heat capacity rates,

$$C_r = \frac{C_{min}}{C_{max}}, \tag{3.4}$$

as well as the exchanger's Number of Transfer Units,

$$NTU = \frac{U \cdot A}{C_{min}}, \tag{3.5}$$

where U is the overall heat transfer coefficient and A is the total heat transfer area. Additionally, the direction of fluid flow changes the method of calculation. In parallel flow heat exchangers the effectiveness is calculated as

$$\epsilon = \frac{1 - \exp\left[-NTU\left(1 + C_r\right)\right]}{1 + C_r} \tag{3.6}$$

while counter flow devices use

$$\epsilon = \frac{1 - \exp\left[-NTU\left(1 - C_r\right)\right]}{1 - C_r \exp\left[-NTU\left(1 - C_r\right)\right]}. \tag{3.7}$$

Once the effectiveness and maximum heat transfer rate are determined, equation 3.3 is used to calculate the actual rate of heat flow, $\dot{Q}$. Finally, the change in temperature for each fluid is calculated based on their respective heat capacity rates at initial conditions and the rate of heat flowing between them. If the change in temperature for either fluid would result in vaporization or condensation, then the values must be recalculated because the specific heat is effectively infinite while the fluid is changing states.

First, the heat flow rate necessary to have the fluid begin changing its state is determined and the fraction of this value relative to the initial heat flow rate is calculated. The heat transfer area is reduced by this fraction and the function is repeated by inputting the state of the two fluids as the one fluid begins to change phase. If enough heat flows between the two fluids such that the one completes the phase change, then the function is repeated a third time with the heat transfer area modified again.

Within this script there are certain assumptions made in order to calculate the output values. The function will not return accurate results if both fluids simultaneously undergo a phase change because the ratio of heat capacities, C_r, will be undefined. Additionally, ambient temperature and associated heat flow to the external environment is not accounted for in the script. Finally, it is assumed the pressure drop from inlet to outlet is negligible for both the high and low temperature fluids.

3.1.2 Expander and Pump

The expander/turbine and pump components are both modeled by a fluid undergoing non-ideal isentropic expansion or compression. For an ideal isentropic process, the fluid will experience some thermodynamic changes while its internal entropy remains constant. During this process, power is produced if the pressure at the inlet is greater than at the outlet, and consumed if inlet pressure is less than that of the outlet. A block diagram of the function can be seen in Figure 3.4.

The function takes as inputs certain properties of the fluid, such as the inlet mass specific enthalpy, h_i ($\mathrm{J\,kg^{-1}}$), both the inlet and outlet pressures, p_i and p_o

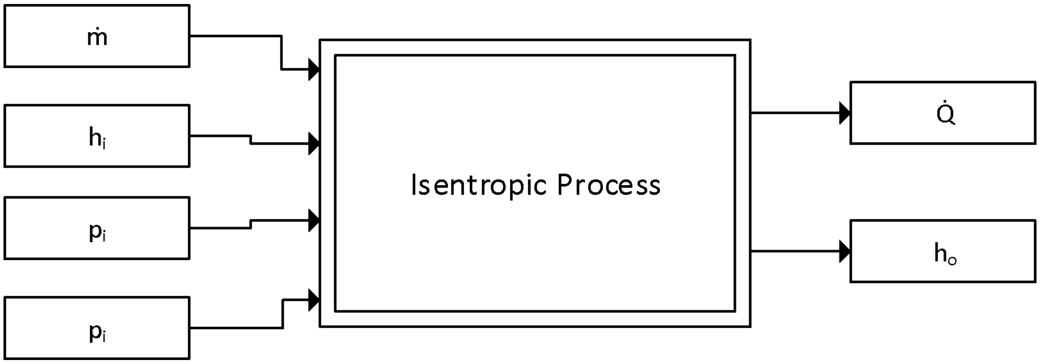

Figure 3.4. Isentropic model diagram showing variable inputs on the left and outputs on the right.

(Pa), and the mass flow rate, $\dot{m}$ ($\mathrm{kg\,s^{-1}}$). Also needed is the fluid CoolProp© handle and the isentropic efficiency, η, a unitless parameter of the machine which describes power loss due to deviations from the ideal isentropic process. The function returns the mechanical power produced or consumed, P (W), and the mass specific enthalpy of the fluid at the outlet, h_o ($\mathrm{J\,kg^{-1}}$).

Using the inputs and the CoolProp© library, the mass specific entropy, S, of the fluid is determined for the fluid at the inlet. In an ideal process this value would remain constant so here it is used to determine the ideal enthalpy of the outlet. Next the ideal power transferred is calculated as

$$P = \dot{m}\left(h_i - h_o\right) \tag{3.8}$$

where h_i and h_o are the inlet and outlet mass specific enthalpies, respectively.

To obtain the mechanical power actually transferred, the isentropic efficiency is applied to the ideal power such that the ideal power is necessarily greater than the actual power. When the value of h_i is larger than h_o, P is positive therefore it is multiplied by efficiency to calculate actual power. When h_i is less than h_o, P is negative so it is divided by efficiency to determine actual power. After the mechanical power is calculated, equation 3.8 is used to find h_o and the fluid temperature at the outlet.

3.2 Induction Generator

The generator block models a squirrel cage induction generator (SCIG) in order to convert the mechanical power to an electrical form. Furthermore, to simulate microgrids with no forms of storage or sources beyond the ORC, it is also self-excited. The model is based off the analysis by Ouazenne et al. of a self excited induction generator in [24] using admittance balancing. It is assumed the active power losses across the core and the excitation capacitance are negligible. Additionally, it is assumed the load is purely active, as any reactive load can be supplied by the conversion device which regulates the frequency and voltage of the microgrid.

The method of admittance balancing relies on the fact that active and reactive power entering and exiting an electrical node must sum to zero. For this analysis, the chosen node is where the rotor, the core, and the combination of the stator, excitation capacitor, and load meet and labeled A in Figure 3.5. Since the voltage across each branch is the same and power flow sums to zero, the admittances must sum to zero as well. By breaking the complex admittances into real and imaginary components, a system of equations can be developed to solve for frequency and core reactance.

The block, seen in Figure 3.6 takes as variable inputs the mechanical power produced by the shaft, P_{mech} (W), and the combined power of the total load and the inverter losses, $P_{total\ load} + P_{inv\ loss}$ (W) as seen by the generator. The block outputs include the gross active power produced, $P_{gen\ gross}$ (W), and the active power losses of the generator, $P_{gen\ loss}$ (W).

To calculate the output variables a function was developed to implement the admittance balancing equations. This function takes the input variables of the rotor speed, n_{mech} (rpm), the combined load as seen by the generator, $P_{total\ load} + P_{inv\ loss}$ (W), and the line to line voltage magnitude, $|V_{ll}|$ (V). The output variables

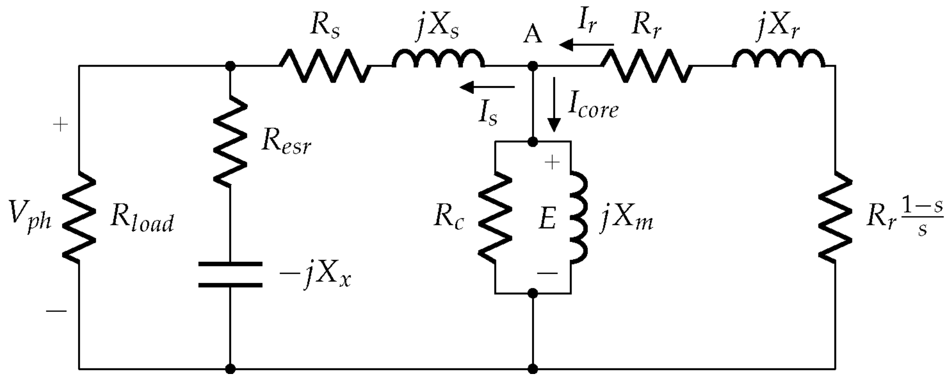

Figure 3.5. Single phase equivalent circuit of a three phase squirrel cage induction machine with a load resistance of R_{load}.

of the function include active power generated, $P_{gen\ gross}$ (W), and internally consumed, $P_{gen\ loss}$ (W), the necessary mechanical power driving the shaft, $P_{mech\ needed}$ (W), and the recalculated line to line voltage magnitude, $|V_{ll}|$ (V). The value of n_{mech} is determined by comparing P_{mech} and $P_{mech\ needed}$ from the previous time step, then integrated with an appropriate proportionality constant, K. This control scheme increases n_{mech} when $P_{mech\ needed}$ is less than P_{mech} and vice versa.

The fixed parameter inputs to the admittance balancing function block are the rated frequency of the machine, f_{rated} (Hz), the number of poles, the resistances and inductances of the rotor, R_r (Ω) and L_r (H), and stator, R_s (Ω) and L_s (H), the external excitation capacitors, C_x (F), coefficients of friction due to bearings, $K_{bearing}$ ($\mathrm{W\,s^{-1}}$), and windage, $K_{windage}$ ($\mathrm{W\,s^{-2}}$), and the magnetization curve comparing the core reactance, X_m (Ω) to the internal voltage across the core, E (V).

A single phase equivalent circuit diagram of the generator which includes these components can be seen in Figure 3.5. R_s and X_s represent the resistive and inductive impedances of the stator. R_r and X_r represent the resistive and inductive impedances of the rotor as referred to the stator. R_c and X_m represent the resistive and inductive impedances due to the magnetization of the core. X_x represents the capacitive impedances of the external excitation capacitor. R_{load} is the active portion of grid load combined with conversion losses of the inverter.

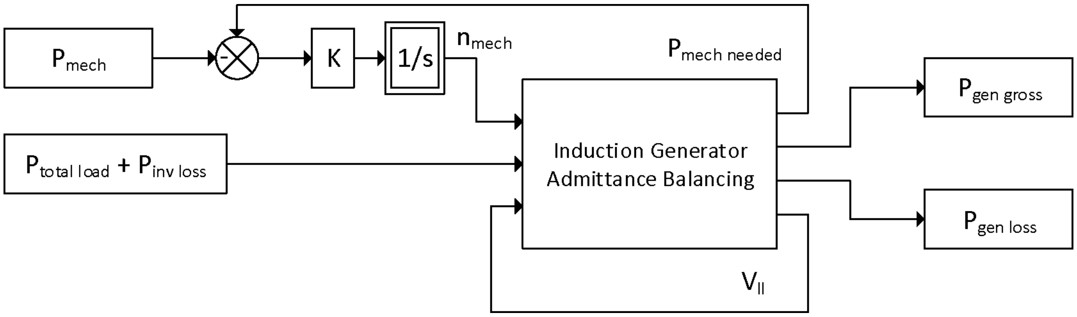

Figure 3.6. Self-excited squirrel cage induction generator model diagram showing variable inputs on the left and outputs on the right.

To determine these outputs, first the rated reactance values of the induction machine are calculated as

$$X = 2\pi f_{rated} L \tag{3.9}$$

and excitation capacitor reactance is calculated as

$$X = \frac{1}{2\pi f_{rated} C}. \tag{3.10}$$

Next, the single phase equivalent load impedance is determined as

$$R_{load} = \frac{V_{ll}^2}{P_{total\ load} + P_{invloss}}. \tag{3.11}$$

The speed of the rotor relative to the synchronous speed is then calculated as

$$b = \frac{n_{mech} poles}{120 f_{rated}}. \tag{3.12}$$

With these values, a system of equations are developed to calculate the frequency and magnetization impedance necessary to balance admittances of the rotor, Y_r, core, Y_m, and combined stator, capacitance, and load branches, Y_s, such that

$$Y_r + Y_m + Y_s = 0. \tag{3.13}$$

Rearranging the real components yields the polynomial

$$K_5 a^5 + K_4 a^4 + K_3 a^3 + K_2 a^2 + K_1 a + K_0 = 0 \tag{3.14}$$

where a is the electrical frequency relative to the synchronous value and K_n is the n^{th} order polynomial coefficient.

Each of the polynomial coefficients are calculated with the reactive impedances under rated frequency conditions as

$$\begin{aligned}
K_5 =& R_r \left(\frac{X_s}{X_x}\right)^2 + R_s \left(\frac{X_r}{X_x}\right)^2 \\
K_4 =& - b\left(K_5 + R_s \left(\frac{X_r}{X_x}\right)^2 \right) \\
K_3 =& R_r \left(\left(\frac{X_s}{R_{load}}\right)^2 + \left(\frac{R_s}{X_x}\right)^2 - 2\frac{X_s}{X_x} \right) + (R_s + R_{load}) \left(\frac{X_r}{R_{load}}\right)^2 \ldots \\
& + R_s \left(\frac{R_r}{X_x}\right)^2 + b^2 R_s \left(\frac{X_r}{X_x}\right)^2 \\
K_2 =& - 2b\,(R_s + R_{load}) \left(\frac{X_r}{R_{load}}\right)^2 - bR_r(\left(\frac{R_s}{X_x}\right)^2 + \left(\frac{X_s}{R_{load}}\right)^2 - 2\frac{X_s}{X_x}) \\
K_1 =& R_r \left(\frac{R_s + R_{load}}{R_{load}}\right)^2 + (R_s + R_{load}) \left(\frac{R2}{R_{load}}\right)^2 + b^2\,(R_s + R_{load}) \left(\frac{X_r}{R_{load}}\right)^2 \\
K_0 =& - bR_r \left(\frac{R_s + R_{load}}{R_{load}}\right)^2 .
\end{aligned}$$

Solving the polynomial yields five possible solutions for a. However, when the values of b, R_r, R_s, R_{load}, X_r, X_s, and X_x are all real and positive, then one of the values is necessarily real and positive [24]. With the real component of the admittance balance equation calculated, Equation 3.13, the imaginary component can be solved to obtain X_m for the rated frequency.

The magnetization curve is then used to determine the corresponding value of E for X_m. If the solved value X_m is outside of the given magnetization curve range, then NaN is returned for the remaining output variables and the simulation fails. Otherwise, the reactive impedances due to inductive and capacitive values are rescaled for the rated frequency such that

$$X = 2\pi a f_{rated} L \tag{3.15}$$

for the inductive components and

$$X = \frac{1}{2\pi a f_{rated} C} \tag{3.16}$$

for the capacitive component. The total impedances of the stator, Z_s, rotor, Z_r, core, Z_{core}, the Thévenin combination of those three branches, $Z_{machine}$, the external excitation branch, Z_{excite}, and the Thévenin combination of all branches, Z_{total}, are calculated as [23]

$$\begin{aligned}
Z_s &= R_s + jX_s \\
Z_r &= R_r \frac{1-s}{s} + R_r + jX_r \\
Z_{core} &= R_c \parallel jX_m \\
Z_{machine} &= R_s + (Z_{core} \parallel Z_r) \\
Z_{excite} &= R_{esr} - jX_x \\
Z_{total} &= Z_{excite} \parallel Z_{machine}.
\end{aligned}$$

Once all the relevant impedances are determined, the currents flowing through the stator, rotor, and core branches are calculated along with the phase voltage across the load. These values are used to determine the output variables. The gross electrical power consumed is calculated as

$$P_{gen\ gross} = 3\frac{V_{ph}^2}{Z_{load}}. \tag{3.17}$$

As previously stated, the active power losses due to resistance in the excitation capacitor and the core are neglected. The active electrical losses through the stator and rotor are calculated as

$$P_s = 3I_s^2 R_s \tag{3.18}$$

and

$$P_r = 3I_s^2R_s, \tag{3.19}$$

respectively. The mechanical losses due to the bearings and windage are calculated as [41]

$$P_{bearing} = \omega_{mech}K_{bearing} \tag{3.20}$$

and [42]

$$P_{windage} = \omega_{mech}^2K_{windage}, \tag{3.21}$$

respectively, where

$$\omega_{mech} = 2\pi\frac{n_{mech}}{60}. \tag{3.22}$$

The total losses of the induction machine are given as

$$P_{gen\ loss} = P_s + P_r + P_{bearing} + P_{windage}. \tag{3.23}$$

The total power generated is combined with the total losses to calculate the mechanical power needed, or

$$P_{mech\ needed} = P_{gen\ gross} + P_{gen\ loss}. \tag{3.24}$$

Finally, the output line to line voltage magnitude is calculated as

$$|V_{ll}| = \sqrt{3}\,|V_{ph}| \tag{3.25}$$

to feed back to the input for the next iteration.

3.3 Inverter

The inverter block is a grid-forming VSI. It converts the unregulated power output from the generator into a form with a stable frequency and voltage. In this model, a simplified view is taken of its operation. The inputs include the inverter's efficiency, η, and the unregulated power output of the induction generator (W). The outputs include the delivered power to the load calculated as

$$P_{out} = \eta P_{gen\ gross} \tag{3.26}$$

and the power loss within the inverter (W) calculated as

$$P_{inv\ loss} = P_{gen\ gross} - P_{out}. \tag{3.27}$$

3.4 Load

The model assumes the microgrid delivers power to a three phase 60 Hz AC load. The total load in the model is determined by the sum of a predefined set point, P_{load}, and the electrical power consumed by the pump used to circulate the working fluid, P_{pump}. The electrical power of the pump is determined by dividing the mechanical power output of the pump model function by the efficiency of the pump driver. In addition to the active load, it is assumed there is a reactive load determined by a predefined power factor parameter. The load seen by the unregulated induction generator is the sum of the total load and the losses due to the inverter.

The total load is combined with both the inverter and generator losses in order to provide the reference for the PI controller. The sum is then compared to the output mechanical power of the ORC system. A gain is applied to the error signal and integrated to provide the desired flow rate of the working fluid. The gain value was selected in order to quickly reach steady state during the simulation. The full diagram of the model, previously seen in Figure 3.1, shows the flow of data from the input variables to the output variables including the induction generator, inverter, and the error control with gain K.

Chapter 4

ORC System Model Validation, Analysis, and Case Study Results

With the ORC prime power system model constructed as described in Chapter 3, simulations were conducted to validate and verify the model. After validation, two case studies, a greenfield and brownfield microgrid, were investigated and analyzed in order to determine whether geothermal ORC generators can be viably used as primary power sources.

4.1 Validation

The model validation is conducted by comparing the results of an ORC test with the simulation results under similar conditions. The test, performed in 2013, is from the University of Alaska Fairbanks and is documented in a report by Lin et al. [43]. The report details the process of testing an Electratherm Green Machine ORC system in a controlled environment at the UAF power plant.

During the sizing of the ORC system, turbine and pump efficiencies, $\eta_{turbine}$ and η_{pump}, as well as heat exchanger areas, A_{evap} and A_{cond}, and transfer coefficients, U_{evap} and U_{cond}, were assumed based off of published values and conventional practice, but final values were not reported. These assumed values are used as the inputs to the model. All of the non-variable ORC prime power system parameters used for the model validation can be seen in Table 4.1.

The only reported electrical parameters of the three phase induction generator were the frequency (60 Hz) and the line to line voltage (480 VAC). The impedance parameters were taken from a 10 HP machine in [24] and scaled based off the expected relative power output. The external excitation capacitance, C_x, was selected in order to yield a terminal voltage roughly equal to the rated voltage. The impedance parameters can be seen in Table 4.2.

Four loads were simulated under different combinations of heat sink flow rates and heat source temperatures and flow rates, as well as high and low pressure values as shown in Table 4.3. For the validation process pressure values used were

Table 4.1. Input parameters for the validation of the ORC prime power system model.

Parameter	Value
U_{evap}	$1500\,\mathrm{W\,K^{-1}\,m^{-2}}$
A_{evap}	$26.5\,\mathrm{m^2}$
U_{cond}	$1400\,\mathrm{W\,K^{-1}\,m^{-2}}$
A_{cond}	$102.5\,\mathrm{m^2}$
$\eta_{turbine}$	0.78
η_{pump}	0.7
$\eta_{pump\ driver}$	0.9
$\eta_{inverter}$	1.0

Table 4.2. Input generator parameters for the validation of the organic Rankine cycle prime power system model.

Parameter	Value
poles	4
f_{rated}	60 Hz
R_s	$0.0279\,\Omega$
X_s	$0.0798\,\Omega$
R_r	$0.0272\,\Omega$
X_r	$0.0475\,\Omega$
C_x	$1000\,\mu\mathrm{F}$
R_{esr}	$0\,\Omega$
K_{bering}	$0.5\,\mathrm{kW\,s^{-1}}$
$K_{windage}$	$0.003\,\mathrm{kW\,s^{-2}}$

based on estimates within reported pressure ranges. The working fluid flow rate was also not reported, and therefore could not be used as an input to the model. Instead the model uses load power set points such that the gross power produced by the simulation approximately matches the reported value and returns the necessary working fluid flow rate to achieve that power output.

Table 4.3. Input variables for the validation of the organic Rankine cycle prime power system model.

	Test			
	1	2	3	4
$T_{source\ in}$(K)	363.9	363.6	353.0	353.9
$T_{sink\ in}$(K)	283.5	284.6	283.6	284.6
$\dot{m}_{source}(\mathrm{kg\,s^{-1}})$	18.3	7.28	18.4	7.35
$\dot{m}_{sink}(\mathrm{kg\,s^{-1}})$	13.0	7.53	13.0	7.54
p_{hi}(kPa)	0.68	0.75	0.60	0.60
p_{low}(kPa)	0.14	0.17	0.14	0.16
$P_{setpoint}$(kW)	35.7	26.0	25.0	19.0

The mechanical power, P_{mech}, the generator power, P_{gen}, inverter output power, P_{out}, and the electrical power consumed by the pump, P_{pump}, of the four tests are plotted in Figure 4.1. Figure 4.2 plots the heat flow rates though the evaporator, $\dot{Q}_{evap}$, and condenser, $\dot{Q}_{cond}$. The inlet and outlet temperatures of the source fluid, $T_{source\ in}$ and $T_{source\ out}$, and sink fluid, $T_{sink\ in}$ and $T_{sink\ out}$, are plotted in Figure 4.3. Table 4.4 compares simulated values in the plots with the measured values from the report.

As desired, the gross electrical power output of the model matches the measured value for each set of inputs. However, the power consumed to run the pump is a factor of 2-3 times greater in the model than what was measured. A pump sizing guide [44] was used to calculate hypothetical hydraulic power needed to move

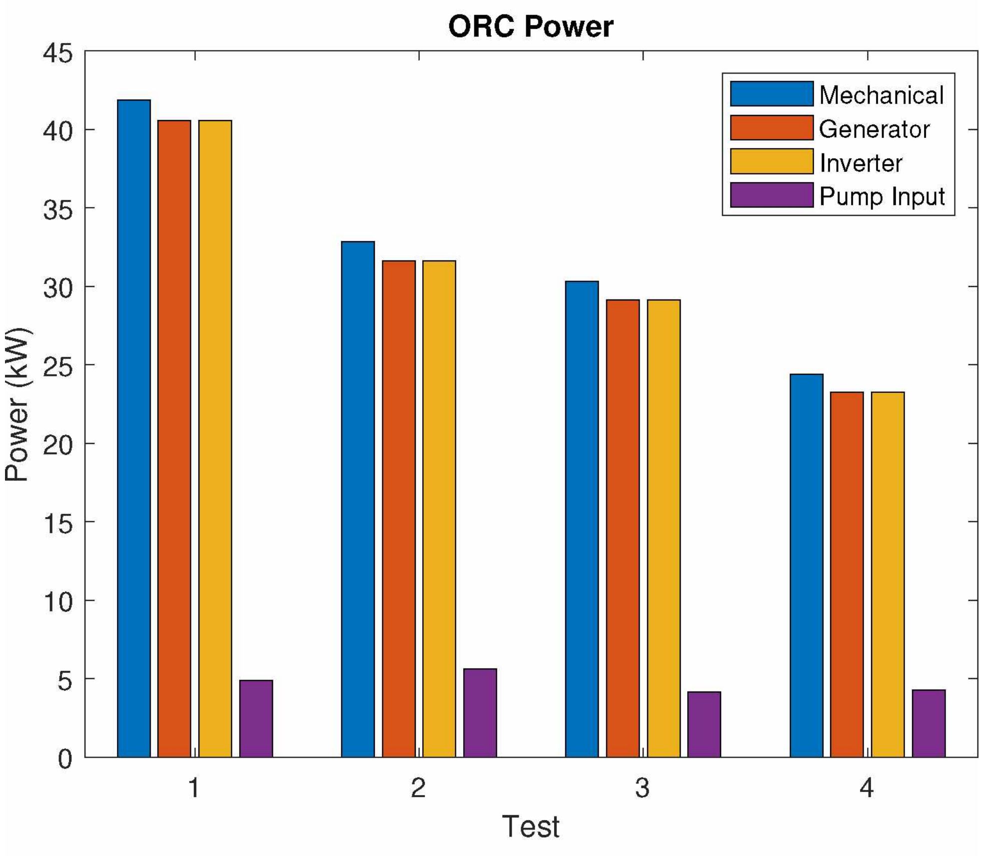

Figure 4.1. Comparison of mechanical power, generator power, inverter output power, and pump power consumption for the validation of the ORC prime power system model. All tests assume a sink temperature of 283 K (10 °C). Tests 1 and 2 use a heat source temperature of 364 K (91 °C), while tests 3 and 4 use 353 K (79 °C). Tests 1 and 3 use a source flow rate of $19\,\mathrm{L\,s^{-1}}$ and a sink flow rate of $13\,\mathrm{L\,s^{-1}}$, where as tests 3 and 4 use a source and sink flow rate of $8\,\mathrm{L\,s^{-1}}$.

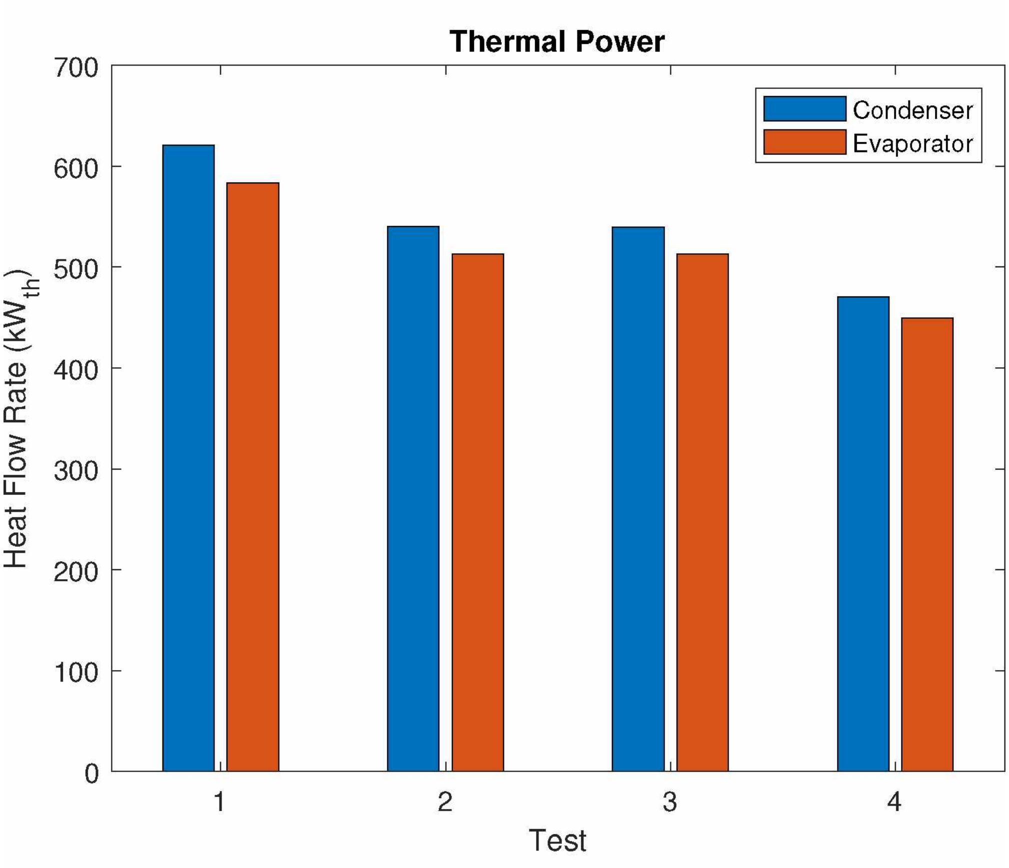

Figure 4.2. Comparison of evaporator and condenser heat flow rates for the validation of the ORC prime power system model. All tests assume a sink temperature of 283 K (10 °C). Tests 1 and 2 use a heat source temperature of 364 K (91 °C), while tests 3 and 4 use 353 K (79 °C). Tests 1 and 3 use a source flow rate of 19 L s^{-1} and a sink flow rate of 13 L s^{-1}, where as tests 3 and 4 use a source and sink flow rate of 8 L s^{-1}.

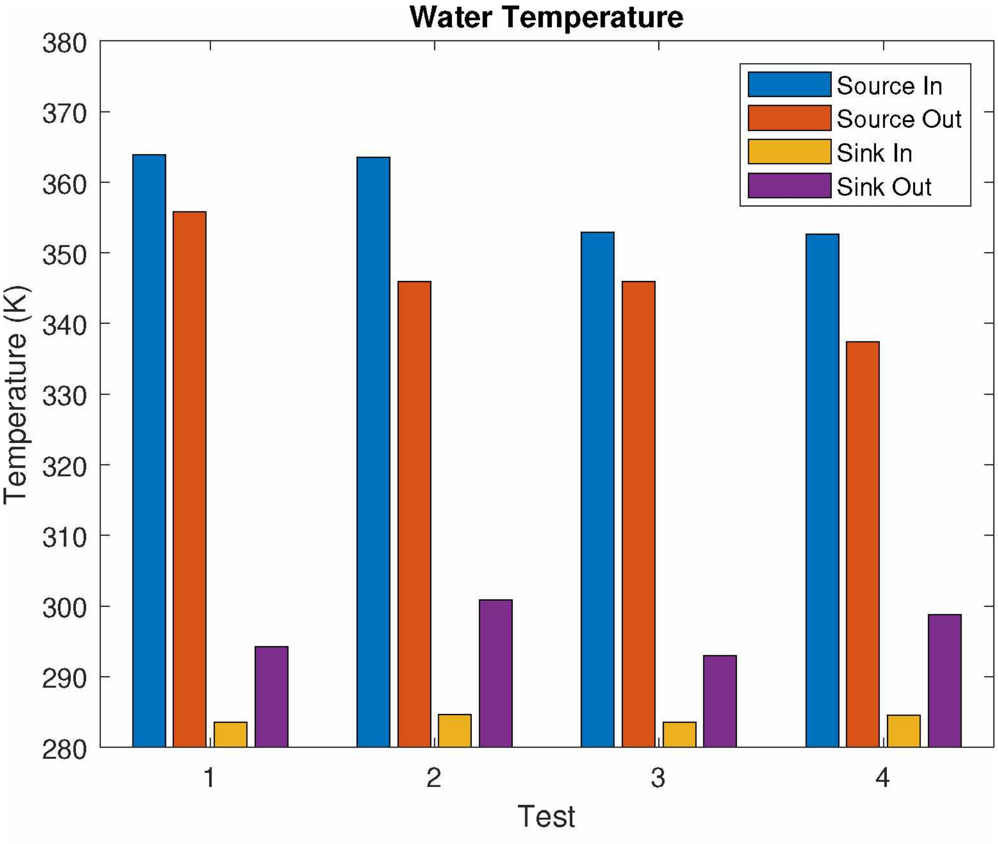

Figure 4.3. Comparison of source and sink inlet and outlet temperatures for the validation of the ORC prime power system model. All tests assume a sink temperature of 283 K (10 °C). Tests 1 and 2 use a heat source temperature of 364 K (91 °C), while tests 3 and 4 use 353 K (79 °C). Tests 1 and 3 use a source flow rate of 19 L s^{-1} and a sink flow rate of 13 L s^{-1}, where as tests 3 and 4 use a source and sink flow rate of 8 L s^{-1}.

Table 4.4. Comparison of output variables for the validation of the ORC prime power system model.

	Test							
	1		2		3		4	
	Meas.	Model	Meas.	Model	Meas.	Model	Meas.	Model
P_{out}(kW)	40.7	40.6	31.8	31.6	29.2	29.2	22.7	23.0
P_{pump}(kW)	2.6	4.9	1.9	5.6	1.5	4.1	1.3	4.2
$\dot{Q}_{evap}$(kW$_{\text{th}}$)	519	621	413	540	393	540	328	466
$\dot{Q}_{cond}$(kW$_{\text{th}}$)	464	583	385	512	356	514	303	446
$T_{source\ out}$(K)	357.2	355.8	350.1	345.9	347.9	346.0	342.0	337.5
$T_{sink\ out}$(K)	292.1	294.2	296.9	300.9	290.1	293.0	294.2	298.7

a liquid at the density of R245-fa across each of the pressure differences listed at the corresponding flow rates. When these hydraulic power values have the assumed pump and drive efficiencies applied as well, they match the pump power values of the model. This indicates the working fluid flow rates of the model are much greater than the operating values measured during the Green Machine ORC system test.

The calculated heat transferred in both the evaporator and the condenser are greater than what was measured in each case. Although the values do tend to follow a similar pattern with higher source temperatures and water flow rates resulting in greater rates of heat transferred. Additionally, the source and sink fluids undergo a greater temperature change in the model as a result of the higher heat flow rates.

Pressure was plotted against enthalpy at various points of the cycle in Figure 4.4 for each of the four tests. The two curves indicate the pressure-enthalpy combinations of R245-fa where the working fluid begins to condense and vaporize. The top-left group of points represents the working fluid state at the outlet of

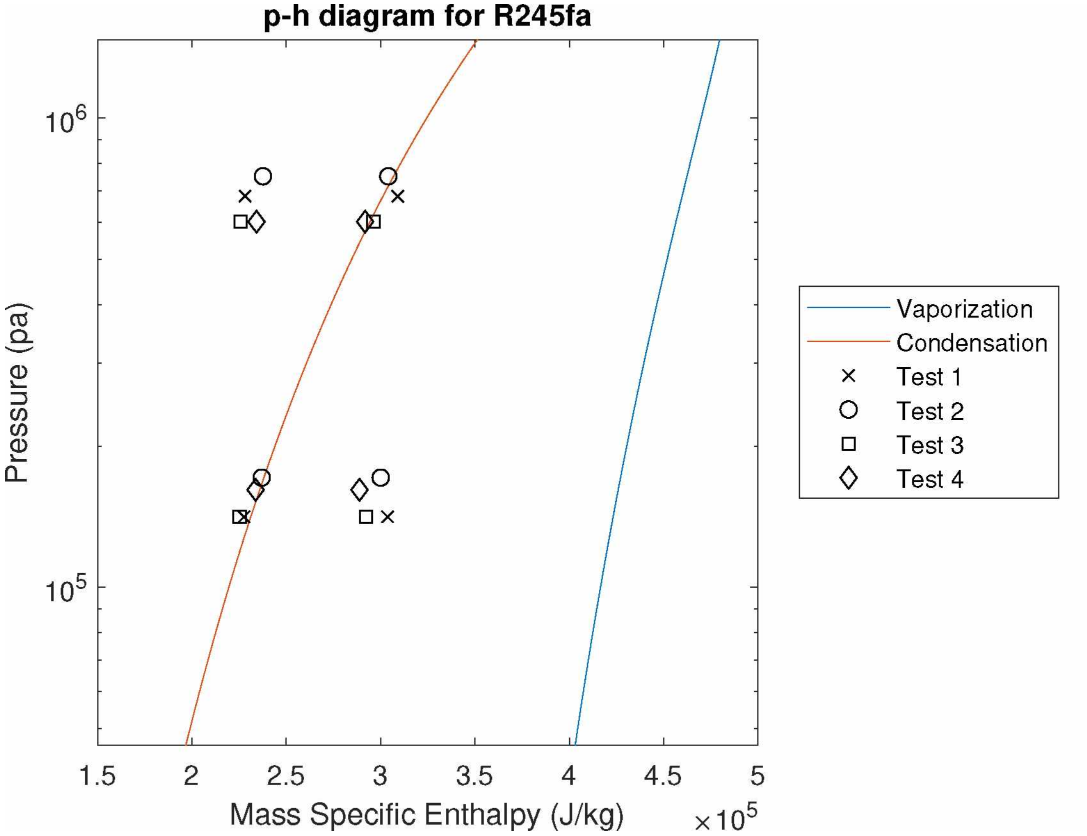

Figure 4.4. Pressure-mass specific enthalpy plot of R245-fa for ORC validation simulation. For tests 1 and 2 $T_{source\ in}$ is about 364 K (91 °C) while for tests 3 and 4 $T_{source\ in}$ is 353 K (79 °C). In all cases $T_{sink\ in}$ is about 283 K (10 °C). The hot water flow rate for tests 1 and 3 are 18.9 L s^{-1} (300 gpm) and 7.6 L s^{-1} (120 gpm) for tests 2 and 4. The cold water flow rate for tests 1 and 3 are 12.6 L s^{-1} (200 gpm) and 7.6 L s^{-1} (120 gpm) for tests 2 and 4.

the pump. The top-right group represents the working fluid state at the inlet of the expander. The bottom-right group represents the working fluid state at the outlet of the expander. Finally, he bottom-left group represents the working fluid state at the inlet of the pump.

For each of these tests, the working fluid just barely begins to boil in the evaporator, if at all. It is expected that the working fluid will either completely vaporize, or at least be further to the right in the liquid-vapor region. Along with the higher than expected pump power, this also indicates that there is more working fluid being pumped throughout the cycle in the model than what was measured.

To re-create conditions where the system outputs are comparable between the modeled and measured values while pumping less fluid, the evaporator area is increased by a factor of four so it is comparable to the area of the condenser. Additionally, the pressure set points are adjusted to values seen in Table 4.5 to account for the new temperatures of the working fluid.

Table 4.5. Input variables for the validation of the ORC prime power system model modified for the adjusted area.

	Test			
	1	2	3	4
p_{hi}(kPa)	0.68	0.68	0.55	0.55
p_{low}(kPa)	0.14	0.14	0.14	0.14
$P_{setpoint}$(kW)	39.6	31.0	28.5	21.9

The results of the second set of validation tests are plotted in Figure 4.5 for the power values, Figure 4.6 for the heat flow rate values, and Figure 4.7 for the water temperature values. Table 4.6 compares the simulation results with the measured results. As expected, the gross output power remained roughly equal to the measured values. The consumed pump power decreased significantly in the new set of tests. Those values are now about half the measured ones, indicating the fluid is

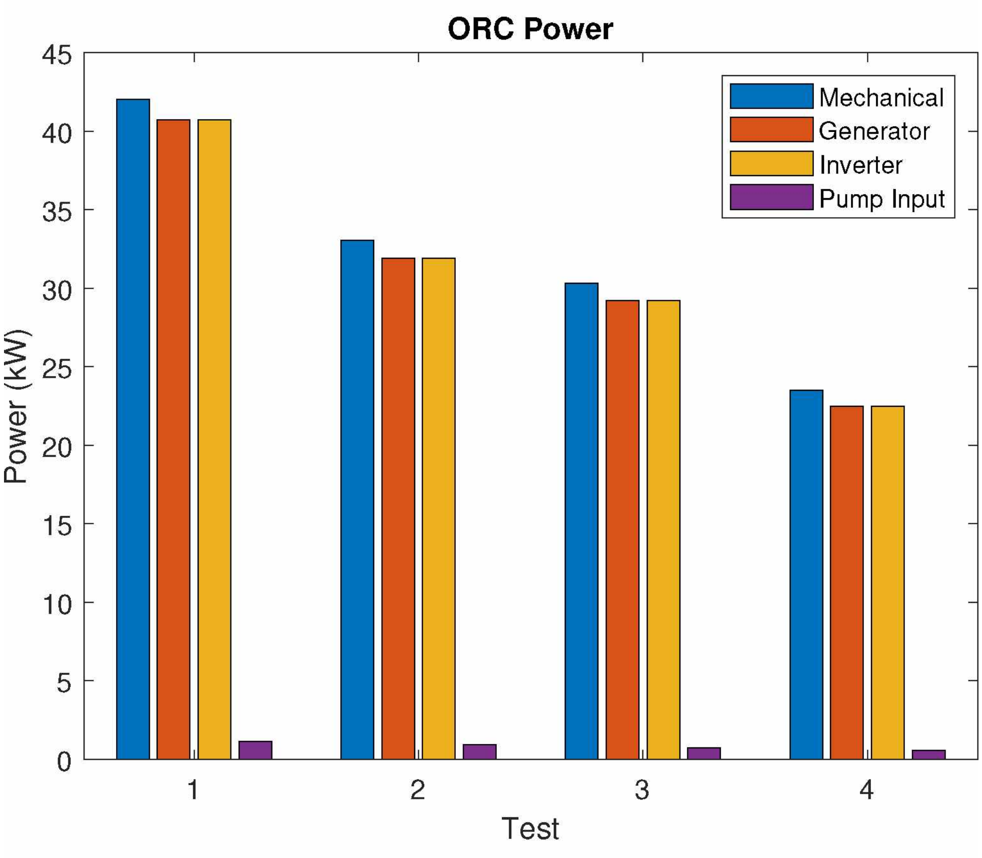

Figure 4.5. Comparison of mechanical power, generator power, inverter output power, and pump power consumption for the validation of the ORC prime power system model with an increased evaporator area. All tests assume a sink temperature of 283 K (10 °C). Tests 1 and 2 use a heat source temperature of 364 K (91 °C), while tests 3 and 4 use 353 K (79 °C). Tests 1 and 3 use a source flow rate of 19 L s^{-1} and a sink flow rate of 13 L s^{-1}, where as tests 3 and 4 use a source and sink flow rate of 8 L s^{-1}.

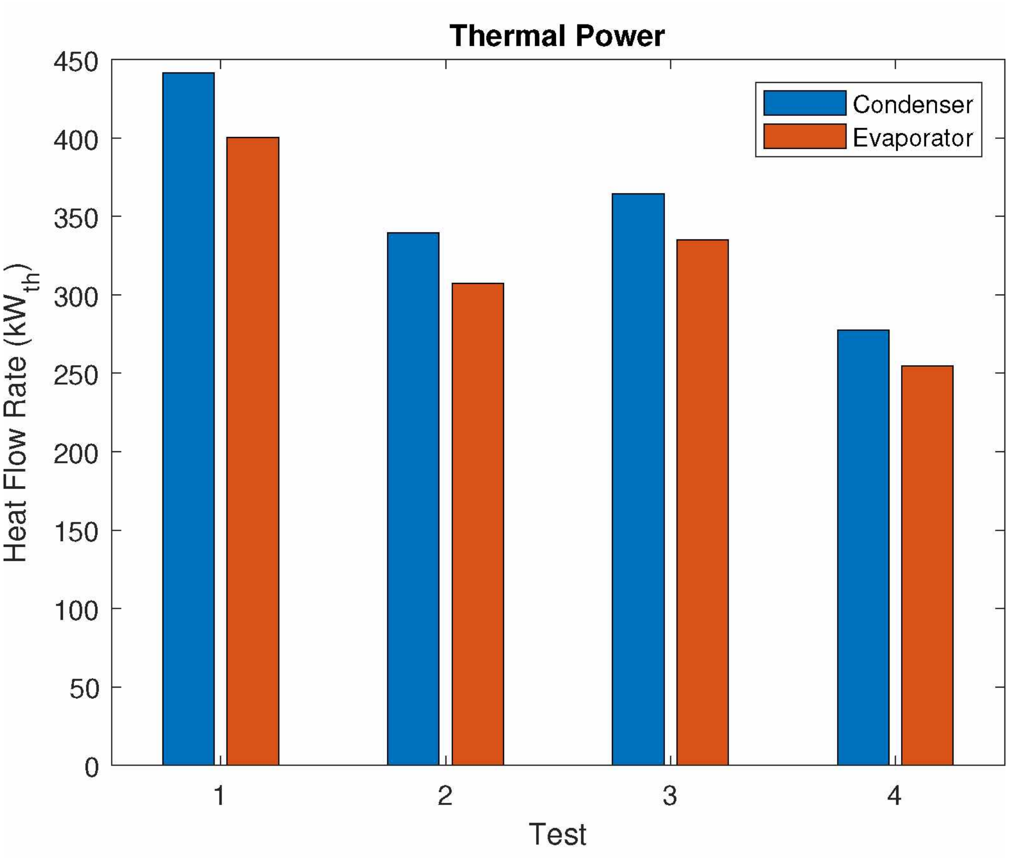

Figure 4.6. Comparison among evaporator and condenser heat flow rates for the validation of the ORC prime power system model with an increased evaporator area. All tests assume a sink temperature of 283 K (10 °C). Tests 1 and 2 use a heat source temperature of 364 K (91 °C), while tests 3 and 4 use 353 K (79 °C). Tests 1 and 3 use a source flow rate of 19 L s^{-1} and a sink flow rate of 13 L s^{-1}, where as tests 3 and 4 use a source and sink flow rate of 8 L s^{-1}.

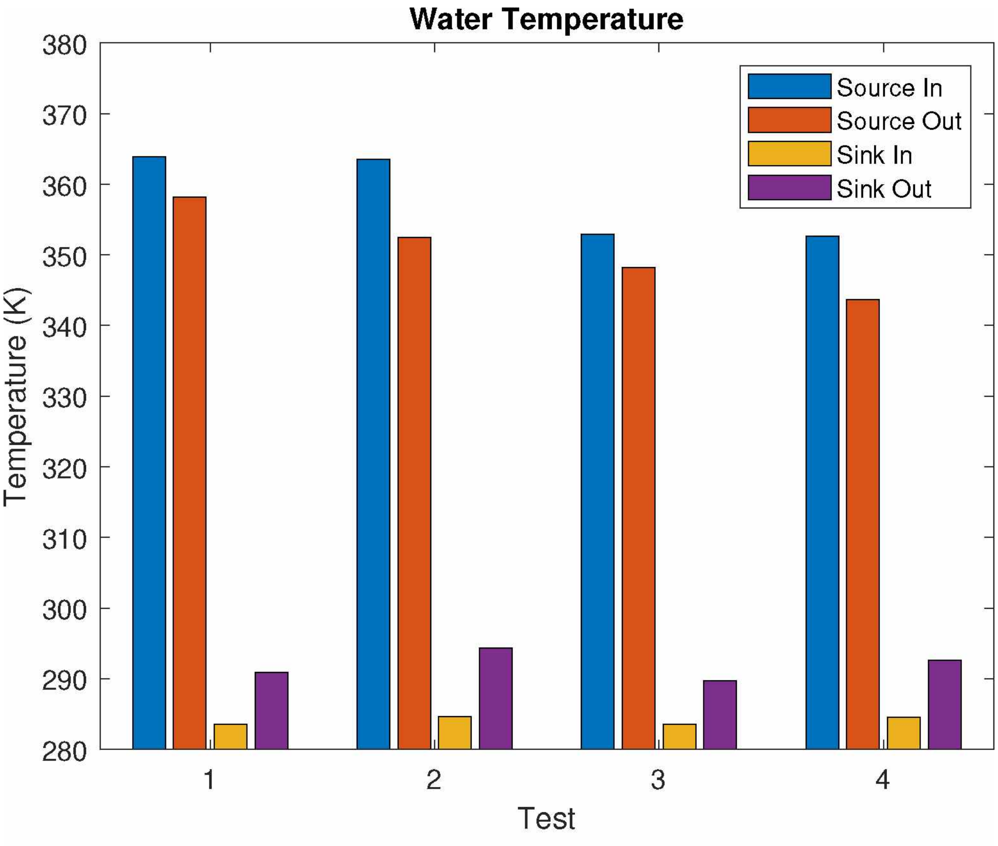

Figure 4.7. Comparison of source and sink inlet and outlet temperatures for the validation of the ORC prime power system model with an increased evaporator area. All tests assume a sink temperature of 283 K (10 °C). Tests 1 and 2 use a heat source temperature of 364 K (91 °C), while tests 3 and 4 use 353 K (79 °C). Tests 1 and 3 use a source flow rate of 19 $\mathrm{L\,s^{-1}}$ and a sink flow rate of 13 $\mathrm{L\,s^{-1}}$, where as tests 3 and 4 use a source and sink flow rate of 8 $\mathrm{L\,s^{-1}}$.

Table 4.6. Comparison of output variables for the validation of the ORC prime power system model with modified evaporator area.

	Test							
	1		2		3		4	
	Meas.	Model	Meas.	Model	Meas.	Model	Meas.	Model
P_{out}(kW)	40.7	40.7	31.8	31.9	29.2	29.2	22.7	22.5
P_{pump}(kW)	2.6	1.1	1.9	0.92	1.5	0.72	1.3	0.55
$\dot{Q}_{evap}(\mathrm{kW_{th}})$	519	441	413	340	393	364	328	277
$\dot{Q}_{cond}(\mathrm{kW_{th}})$	464	400	385	307	356	335	303	254
$T_{source\ out}$(K)	357.2	358.2	350.1	352.5	347.9	348.2	342.0	343.7
$T_{sink\ out}$(K)	292.1	290.9	296.9	294.4	290.1	289.7	294.2	292.6

moving at a slower rate. The thermal power measurements are now greater than the simulated values by about $30\,\mathrm{kW_{th}}$ to $80\,\mathrm{kW_{th}}$ and the source and sink outlet temperatures are correspondingly higher and lower, respectively. Additionally, Figure 4.8 shows the lower mass flow rate of the working fluid allows it to fully vaporize due to the larger transfer area of the evaporator.

Under four different combinations of source and sink flow rates and temperatures, the gross output power of the model matched the measured values. However, given the assumed heat transfer area of the evaporator and condenser, the power consumed by the pump was calculated to be much greater than what was measured. Increasing the area of the evaporator such that it roughly matched the condenser greatly reduced the calculated power needed by the pump. However, this is not typical for ORCs. Generally condensers are sized larger than evaporators so the system can also feasibly use air to cool the working fluid.

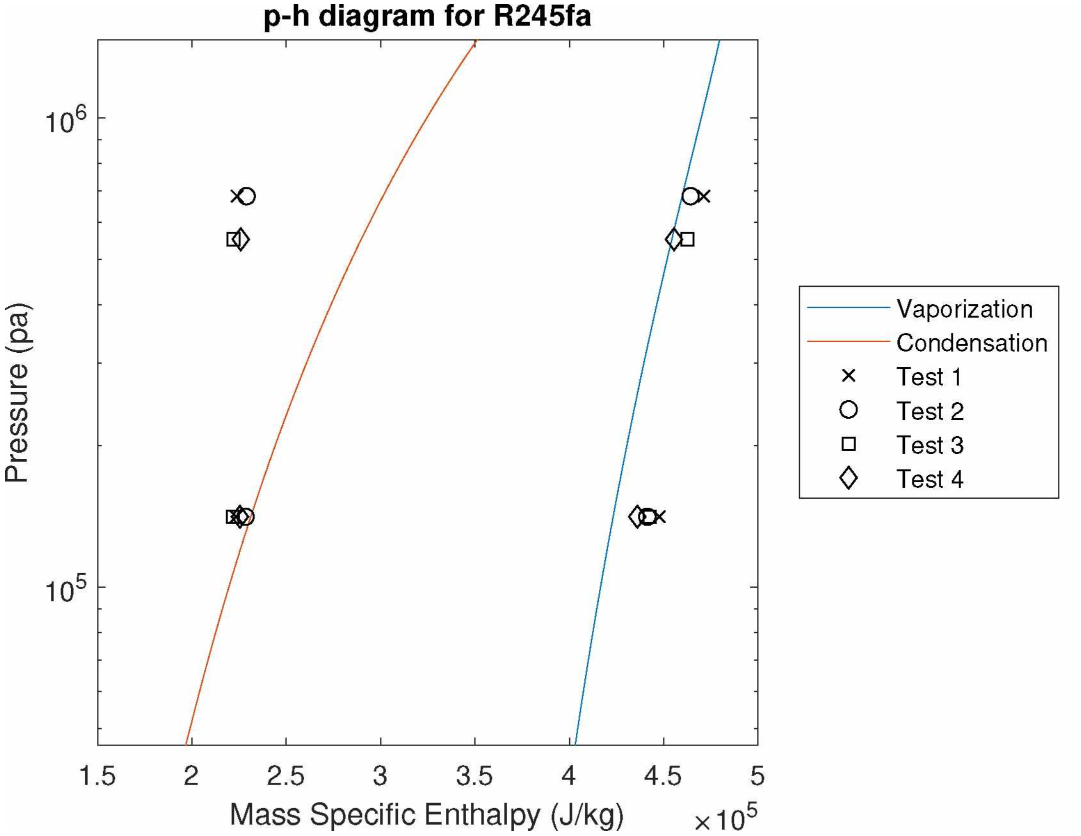

Figure 4.8. Pressure-mass specific enthalpy plot of R245-fa for ORC validation with an over sized evaporator area. Input temperatures and flow rates remain the same. For tests 1 and 2 $T_{source\ in}$ is about 364 K (91 °C) while for tests 3 and 4 $T_{source\ in}$ is 353 K (79 °C). In all cases $T_{sink\ in}$ is about 283 K (10 °C). The hot water flow rate for tests 1 and 3 are 18.9 L s^{-1} (300 gpm) and 7.6 L s^{-1} (120 gpm) for tests 2 and 4. The cold water flow rate for tests 1 and 3 are 12.6 L s^{-1} (200 gpm) and 7.6 L s^{-1} (120 gpm) for tests 2 and 4.

4.2 Case Study Scenarios

With the model validated the greenfield and brownfield scenarios can be simulated and analyzed. For the former, no electrical grid is currently present, while for the latter there is existing electrical infrastructure. However, in the brownfield case the grid is not perfectly reliable. In the event of a grid outage, the microgrid should be capable of disconnecting and acting on its own. In both scenarios, the same generator impedances are used as in the validation simulations.

4.2.1 Greenfield Scenario — Alaska

This system is located approximately two hours north of Nome, Alaska on the western coast of the state as seen Figure 4.9, a geothermal heat map of Alaska [45]. The hot water resource is drawn from the Pilgrim Hot Springs. The hot water is assumed to be drawn at a temperature of 364.5 K (91.3 °C) and a flow rate of 15.2 $\mathrm{L\,s^{-1}}$. The hot water resource is fairly stable throughout the year. The low temperature water ranges from 276.6 K to 281.6 K (3.5 °C to 8.5 °C) at a flow rate of 15.6 $\mathrm{L\,s^{-1}}$ to provide a heat sink [46, 47]. Though the low temperature sink resource does vary in temperature with the seasons, the nearby geothermal activity keeps it liquid all year round.

The assumed working fluid is R245-fa, a typical refrigerant used by a large proportion of ORC manufacturers. The operating high and low pressure set points of the working fluid are 570 kPa to 600 kPa and 130 kPa to 140 kPa, respectively. The evaporator has a heat transfer area of 37.8 $\mathrm{m^2}$, and an effective heat transfer coefficient of 1500 $\mathrm{W\,K^{-1}\,m^{-2}}$. The condenser has an area of 102.5 $\mathrm{m^2}$, but an effective heat transfer coefficient of 1400 $\mathrm{W\,K^{-1}\,m^{-2}}$.

Four tests were conducted under different input conditions. Tests one and two use the warmer summer heat sink temperature, while tests three and four use the colder winter heat sink temperatures. Furthermore, tests one and three use the maximum power setpoint while also ensuring the working fluid fully evaporates in the evaporator, whereas in tests two and four the maxiumum power setpoint

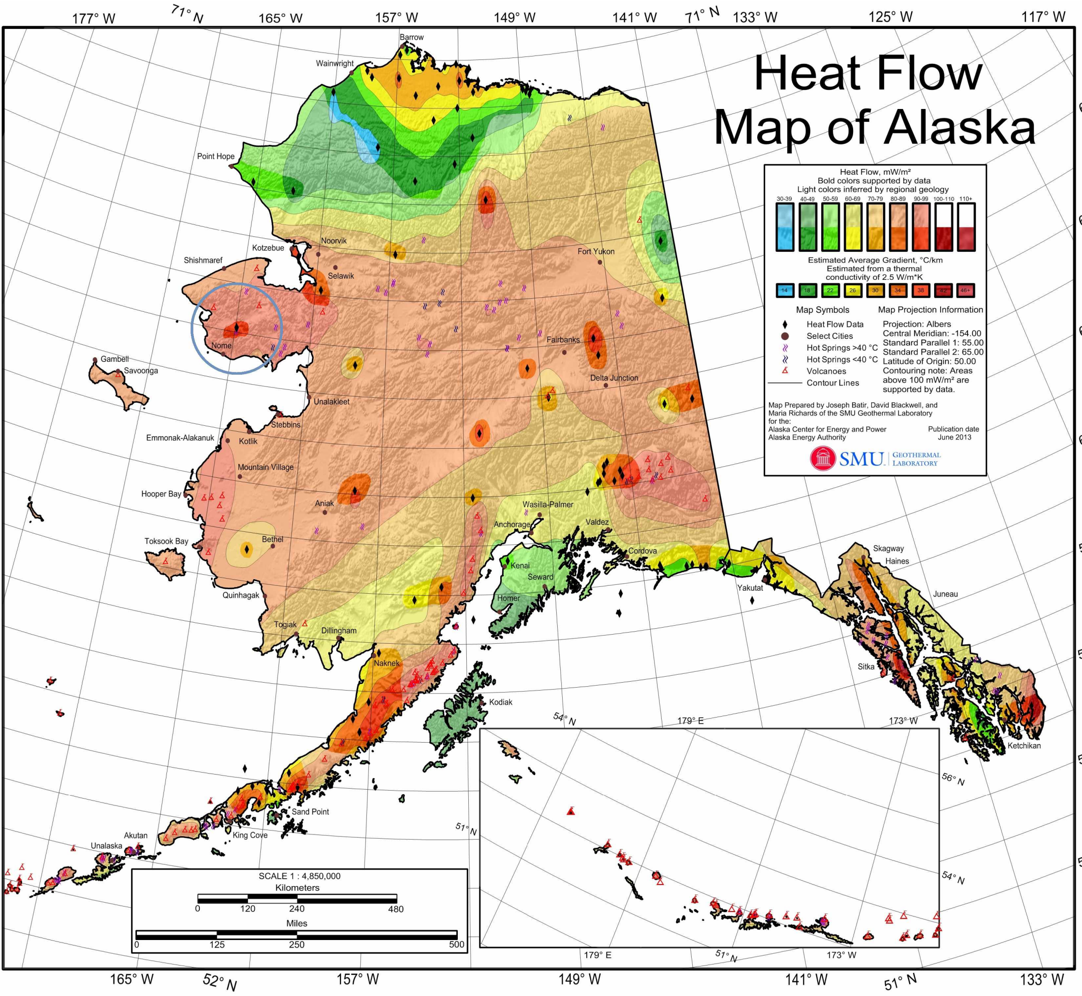

Figure 4.9. A heat map of Alaska indicating geothermal hot spots within the state. The Pilgrim Hot Springs circled in blue. Credit: Batir et al. [45].

with a stable simulation is used. Figure 4.10 compares the mechanical power, P_{mech}, the generator power, P_{gen}, inverter output power, P_{out}, and the electrical power consumed by the pump, P_{pump}, for the different tests. The working fluid mass flow rates, $\dot{m}$, are seen in Figure 4.11. Finally, the heat flow rates of the evaporator and condenser, $\dot{Q}_{evap}$ and $\dot{Q}_{cond}$, are seen in Figure 4.12.

Depending on the operator's tolerance of the state of the working fluid, the available gross output of the ORC prime power system can vary significantly. The gross output power of the inverter, P_{out}, the system can achieve while ensuring the working fluid fully vaporizes is 28.3 kW to 31.6 kW throughout the year. In these cases the pump only needs to move about $1.6\,\mathrm{kg\,s^{-1}}$ consuming 0.80 kW of power. This yields a net output of 27.5 kW to 30.8 kW before accounting for the power required for hot and cold water pumps. Heat is absorbed from hot water at a rate, $\dot{Q}_{evap}$, of $361\,\mathrm{kW_{th}}$ to $406\,\mathrm{kW_{th}}$ indicating a net efficiency

$$\eta = \frac{P_{out} - P_{pump}}{\dot{Q}_{evap}} \tag{4.1}$$

of $\eta = 7.6\%$.

More heat can be moved by increasing the working fluid flow rate yielding a greater gross power output. For flow rates of around $8.4\,\mathrm{kg\,s^{-1}}$, the gross power output of the system is 44.6 kW to 46.2 kW, with the greater end of the range occurring during the winter. Under these conditions the pump consumes about 4.5 kW cycling the working fluid, netting a power output of 40.1 kW to 41.7 kW. More power is being generated because heat is being transferred at a greater rate from the source, $751\,\mathrm{kW_{th}}$ to $792\,\mathrm{kW_{th}}$, but the efficiency is lower at about 5.3%.

The drop in efficiency from 7.6% to 5.3% as the working fluid flow rate increases can be understood by the plots in Figure 4.13. These plots show pressure versus temperature, pressure versus mass specific enthalpy, and temperature versus mass specific entropy using summer and winter relative ambient temperature conditions at the site. The curves in the plots represent the dividing lines between pure liquid on the left side of each plot, pure gaseous on the right, and the region

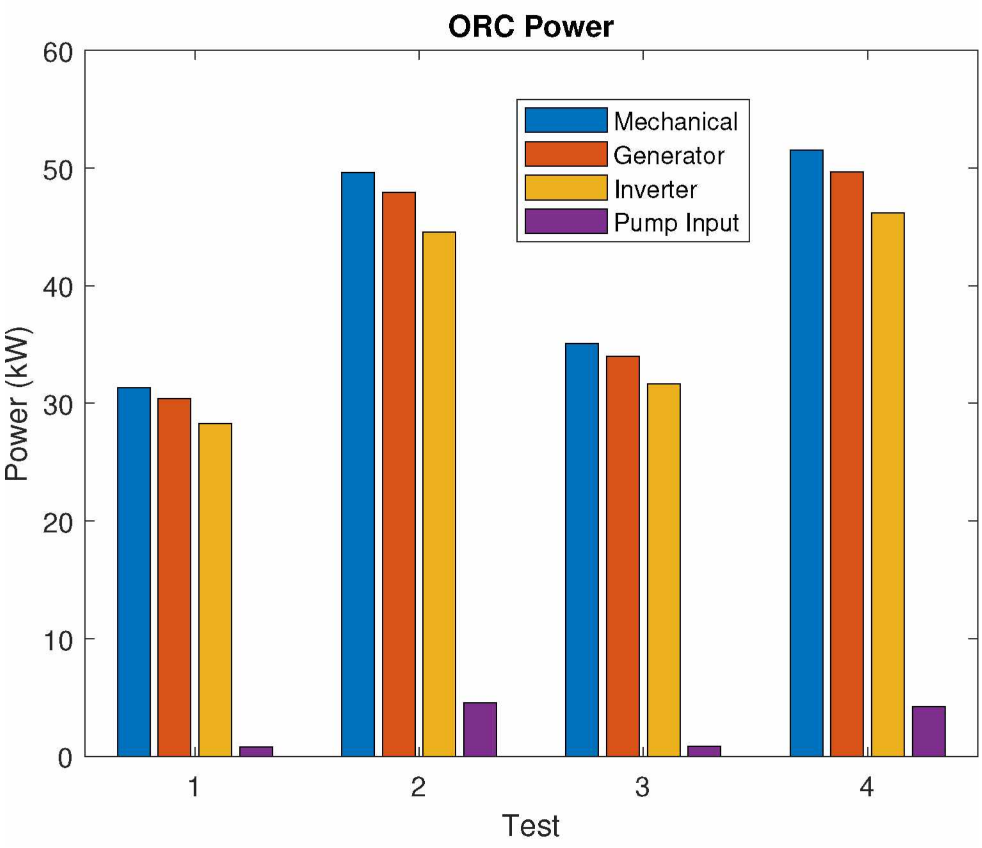

Figure 4.10. Comparison of mechanical power, generator power, inverter output power, and pump power consumption for the greenfield case of the ORC prime power system model. All tests assume a source temperature of 364.5 K (91 °C), and source and sink flow rates of 940 L min^{-1}. Tests 1 and 2 use a heat sink temperature of 281.6 K (8.5 °C), while tests 3 and 4 use 276.6 K (3.5 °C). The power setpoints of the four tests are 27.5 kW, 40.0 kW, 30.8 kW and 42.0 kW. Tests 1 and 3 use the maximum power setpoint while also ensuring the working fluid fully evaporates in the evaporator. Tests 2 and 4 use the maximum power setpoint while maintaining a stable simulation.

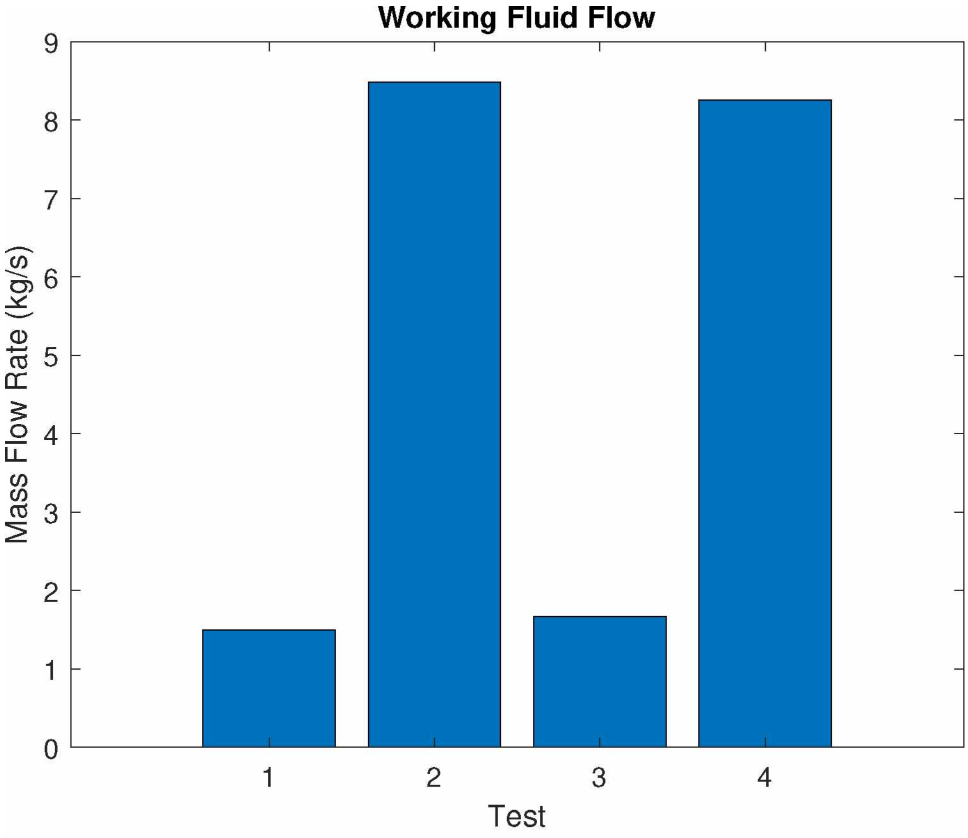

Figure 4.11. Comparison of working fluid mass flow rates for the greenfield case of the ORC prime power system model. All test assume a source temperatures of 364.5 K (91 °C), and source and sink flow rates of 940 L min^{-1}. Tests 1 and 2 use a heat sink temperature of 281.6 K (8.5 °C), while tests 3 and 4 use 276.6 K (3.5 °C). The power setpoints of the four tests are 27.5 kW, 40.0 kW, 30.8 kW and 42.0 kW. Tests 1 and 3 use the maximum power setpoint while also ensuring the working fluid fully evaporates in the evaporator. Tests 2 and 4 use the maximum power setpoint while maintaining a stable simulation.

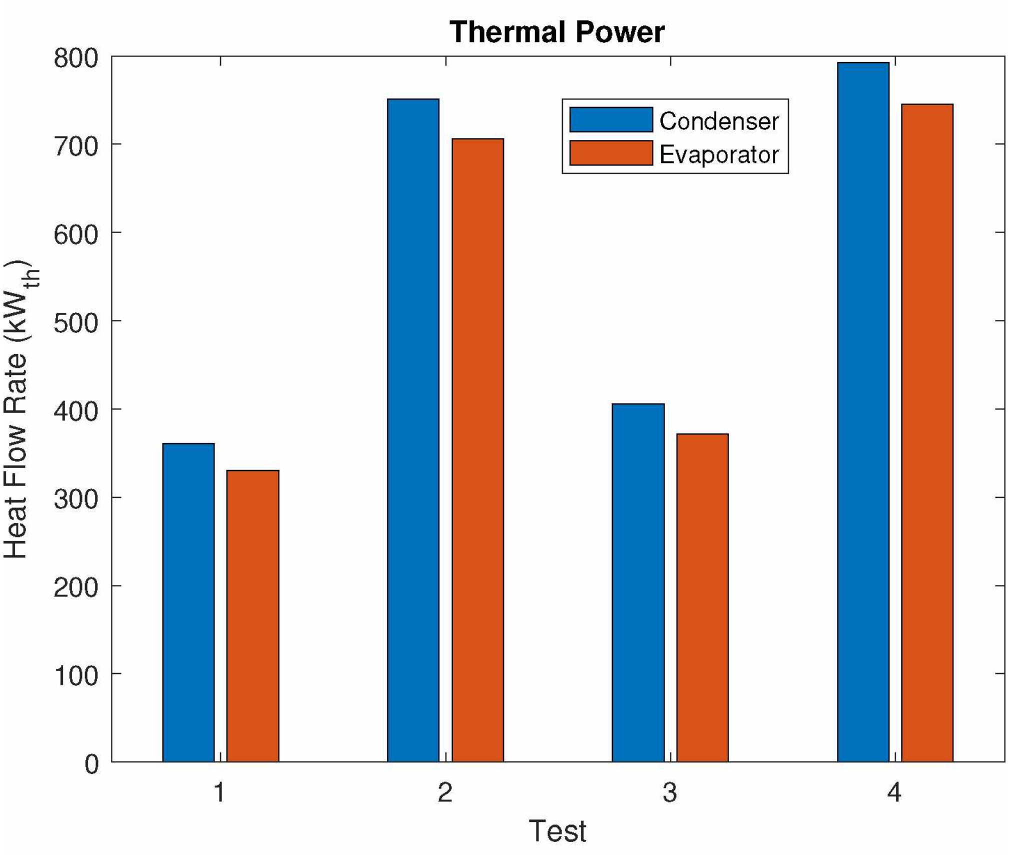

Figure 4.12. Comparison among heat flow rates through the evaporator and condenser for the greenfield ORC prime power system model. All test assume a source temperatures of 364.5 K (91 °C), and source and sink flow rates of 940 L min^{-1}. Tests 1 and 2 use a heat sink temperature of 281.6 K (8.5 °C), while tests 3 and 4 use 276.6 K (3.5 °C). The power setpoints of the four tests are 27.5 kW, 40.0 kW, 30.8 kW and 42.0 kW. Tests 1 and 3 use the maximum power setpoint while also ensuring the working fluid fully evaporates in the evaporator. Tests 2 and 4 use the maximum power setpoint while maintaining a stable simulation.

where the fluid overcomes the latent heat necessary to change states in-between the curves. The points, with data markers in each of the three plots, represent the state of the working fluid between each block for the four different tests: low working fluid flow rate during summer, high flow rate during summer, low flow rate in winter, and high flow rate in winter.

The first panel (top) shows pressure (Pa) versus temperature (K). A benefit of this plot is that it is easy to identify increases and decreases in both temperature and pressure as the working fluid moves through the cycle. However, this comes at a cost of resolution in the liquid-vapor region. In this plot the vaporization and condensation curve overlap without representing the latent heat needed to change from one phase to the other. In this particular plot there are points in this area that are not discernible despite being at different energy levels.

The second panel (middle) helps resolve this problem by plotting mass specific enthalpy (J/kg) on the x-axis instead of temperature. It can be seen that the low flow rate tests allow the fluid to fully become a gas and cross the vaporization curve. Since each kg of fluid contains more energy, the turbine is able to operate more efficiently, even though more total energy is being extracted at higher flow rates.

The third panel (bottom) shows temperature (K) as a function of mass specifc entropy (J/(kg K)). This shows the non-ideal isentropic transition of the pump and turbine. This is difficult to see for the pump because the points before and after the pump lie nearly on top of one another. Both the temperature and entropy changed very little in the process. In the turbine, however, it is clearer. Ideally the points would drop straight down on this plot, but instead there is a slight increase in entropy due to the isentropic inefficiency as expected from the 2^{nd} law of thermodynamics.

The 30.8 kW power output could be used to operate a greenhouse nearby during the winter. Assuming about 1 kW of power to supply the circulation fans and watering system, as well as LED lighting of $650\,\mathrm{W\,m^{-2}}$ [48] for growing plants such

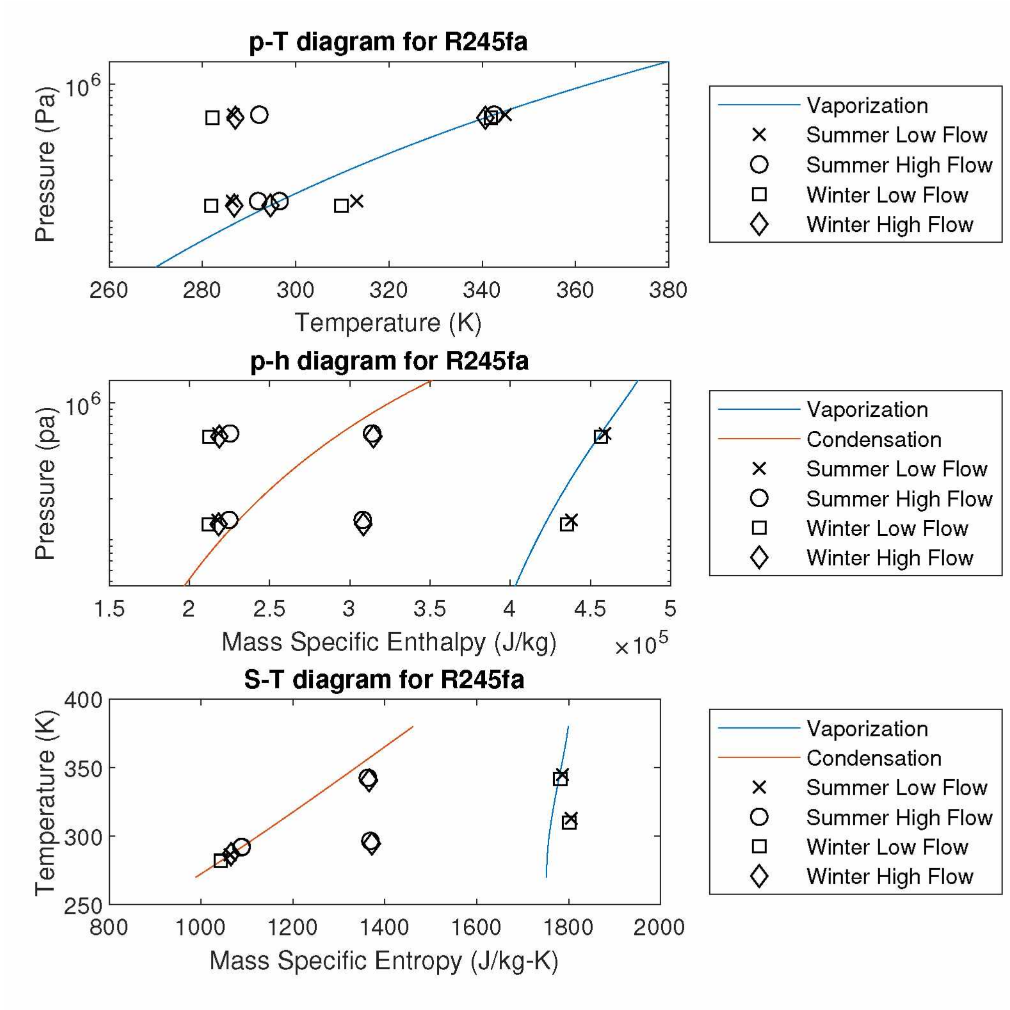

Figure 4.13. Thermodynamic plots from the greenfield ORC prime power system which includes pressure against temperature (top), pressure against mass specific enthalpy (middle), and temperature against mass specific entropy (bottom). All points assume a source temperatures of 364.5 K (91 °C), as well as source and sink flow rates of 940 L min^{-1}. Sink temperatures are assumed to be 276.6 K (3.5 °C) in Winter and 281.6 K (8.5 °C) in Summer. High flow rate points have a working fluid mass flow rate of approximately 8.4 kg s^{-1}

as lettuce and radish, then a roughly 45 m^2 greenhouse could be powered entirely off the ORC system. During the summer months fewer lights, if any, are needed to grow the plants due to the longer Alaska days, therefore, the lower available power would not be a problem.

4.2.2 Brownfield Scenario — Iceland

Bergstaðir, Iceland is located inland east of Reykjavík, as seen by the circled region on the map in Figure 4.14, which depicts high and low temperature geothermal resources on the island [49]. The hot water resource is drawn at a flow rate of about 6 $\mathrm{L\,s^{-1}}$ from below the surface to a holding tank before being distributed to the homes for heating. While sitting in this tank, the water is approximately 368 K (95 °C). Nearby there is a 278 K (5 °C) stream which can be drawn from in order to provide a low temperature sink fluid.

The working fluid is also assumed to be R245-fa. The operating high and low pressure set points of the working fluid are 600 kPa and 140 kPa, respectively. The evaporator has a heat transfer area of 37.83 m^2, and an effective heat transfer coefficient of 1500 $\mathrm{W\,K^{-1}\,m^{-2}}$. As before, it is usual in commercial ORC systems for the condenser to have a greater area to allow for the option of air cooling. In this case the condenser has an area of 37.83 m^2 and an effective heat transfer coefficient of 1400 $\mathrm{W\,K^{-1}\,m^{-2}}$. The pump and its driving motor are assumed to have efficiencies of 70% and 90%, respectively. The turbine is assumed to have a mechanical efficiency of 78% for the operating conditions. The inverter used to convert the unregulated AC output of the self-excited induction generator to a regulated voltage output at 60 Hz is assumed to have an efficiency of 93%.

Under these conditions, the model predicts an ORC prime power system to produce 31.7 kW of mechanical power, 30.8 kW of electrical power from the induction generator, a gross electrical power output from the inverter of 28.6 kW, and a working fluid pump power consumption of 0.8 kW as shown in Figure 4.15. After accounting for the power consumed to circulate the working fluid, the resultant

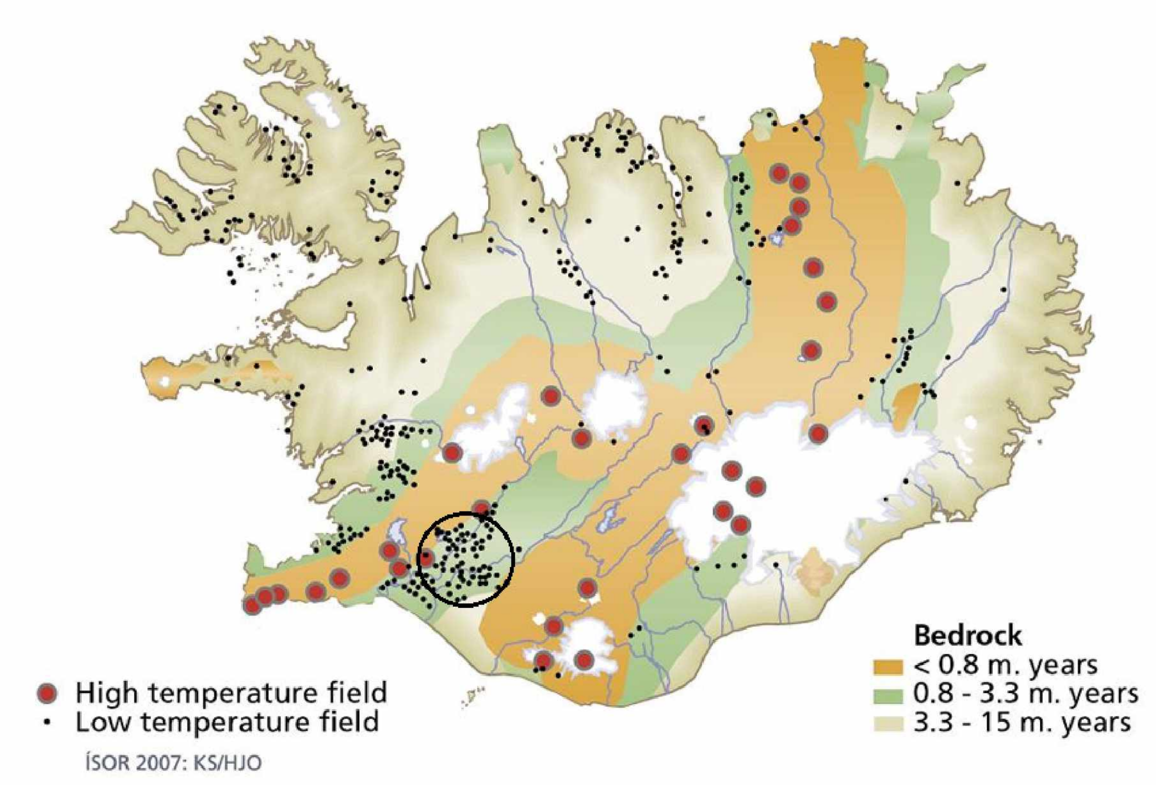

Figure 4.14. A heat map of Iceland indicating high and low temperature geothermal hot spots within the country. Bergstaðir is located in the region circled in black. Credit: Loftsdottir et al. [49].

power available for other devices on the microgrid is 27.8 kW. Unfortunately, this is insufficient for the desired application of this system; running two 15 kW motors used to distribute the hot water for home heating. Additionally, this does not even take into account the pump needed to collect the low-temperature stream water for the low temperature sink.

Figure 4.16 shows similar thermodynamic plots as for the greenfield scenario. The top right point of each plot represents the state of the working fluid as it is leaving the evaporator before entering the expander. It can be seen that this point lies on the vaporization curve. This means if the working fluid mass flow rate were to increase in order to get more power out, then the fluid would not fully vaporize and the expander efficiency assumption would no longer be valid. If the amount of heat transferred could be increased, then it is possible the working fluid flow rate could increase as well while maintaining full vaporization. This can be achieved by increasing the heat transfer area of the evaporator. Additionally, different working fluids have different the latent heats, heat capacities, and evaporation temperatures, all of which affect the heat transfer rate.

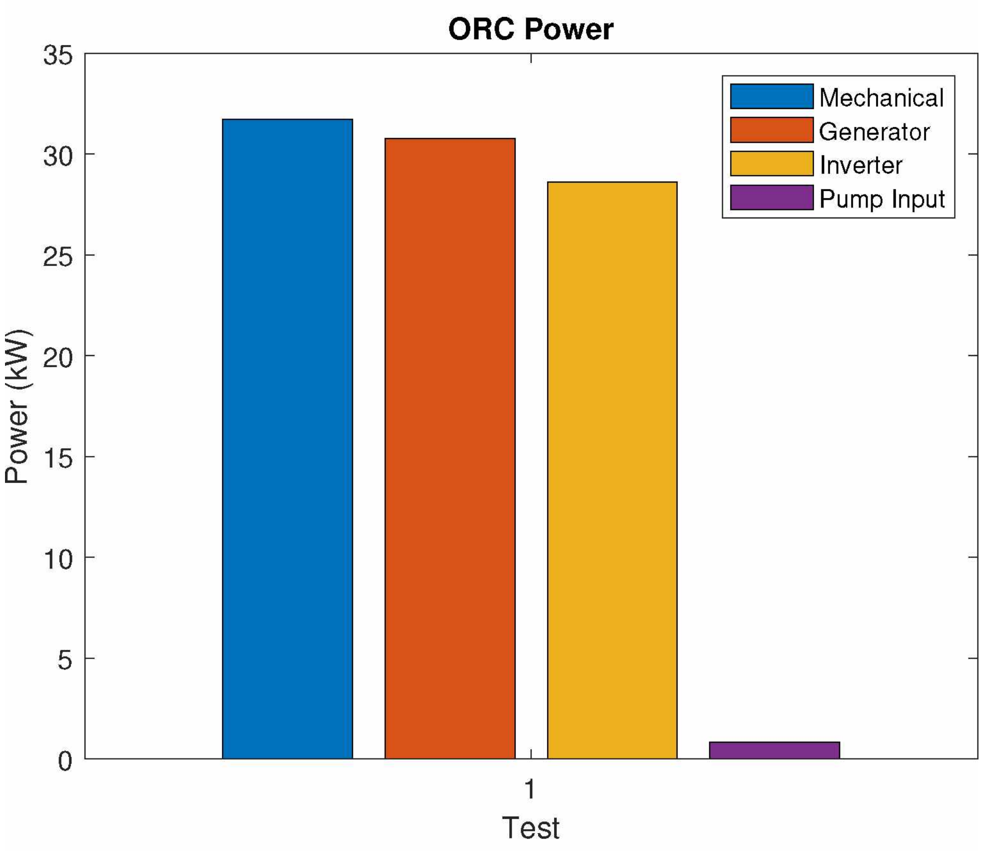

Figure 4.15. Comparison of mechanical power, generator power, inverter output power, and pump power consumption for the brownfield case of the ORC prime power system model. The test assumes a source temperature of 368 K (95 °C) and a sink temperature of 278 K (5 °C). The source is assumed to flow at a rate of $6\,\mathrm{L\,min^{-1}}$ while the sink flows at $7\,\mathrm{L\,min^{-1}}$.

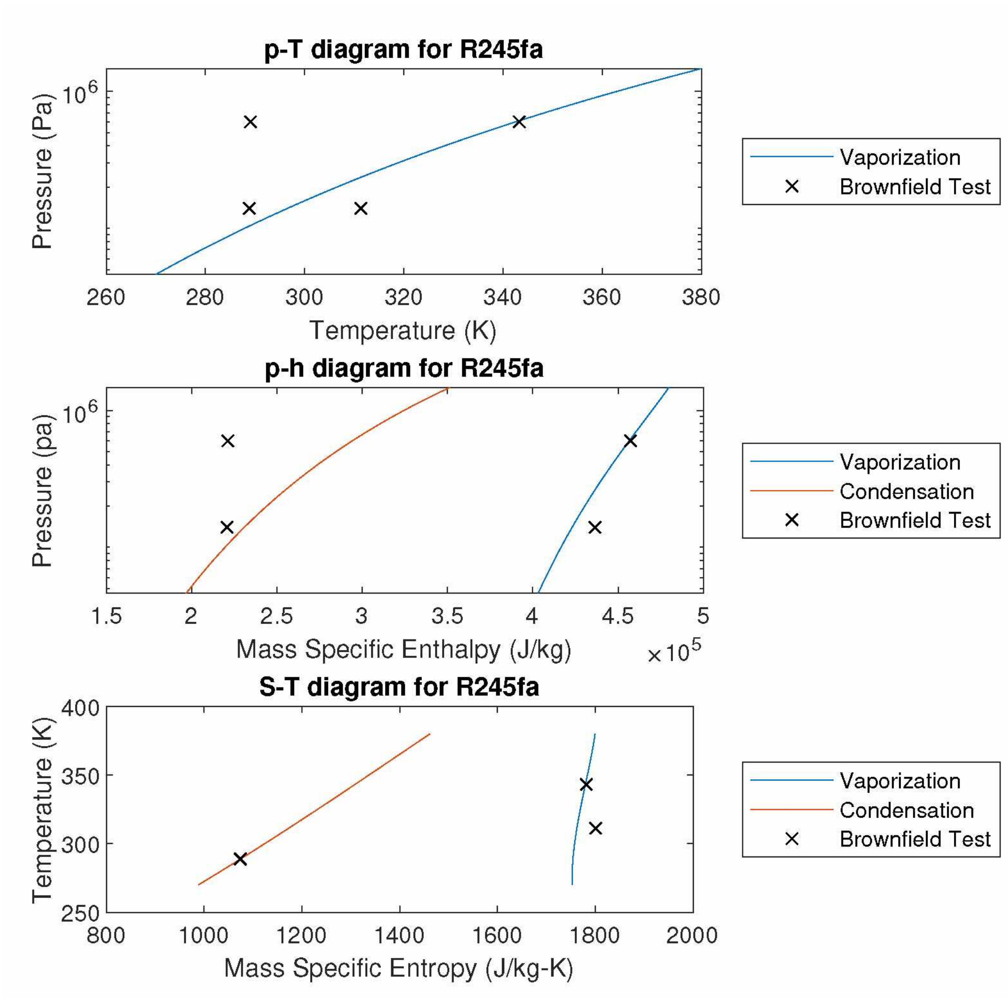

Figure 4.16. Thermodynamic plots from the simulated brownfield ORC prime power system plotting pressure against temperature (top), pressure against mass specific enthalpy (middle), and temperature against mass specific entropy (bottom). Source temperature and flow rate are assumed to be 368 K (95 °C) and 6 L s^{-1}. Sink temperature and flow rate are assumed to be 278 K (5 °C) and 7 L s^{-1}.

Chapter 5

Conclusions and Future Work

The goal of this thesis was to explore a viable and affordable method of incorporating geothermal energy as a prime power source to form a microgrid using an organic Rankine cycle system and an induction generator. Low temperature geothermal sites were looked at specifically because such sites can be found within Alaska and similar high latitude environments which are not fully utilized at this time. In order to explore the feasibility of such systems, a model was developed to simulate the thermodynamic and electrical processes of the ORC and the induction generator. Two different systems were examined as case studies: a greenfield site with minimal existing infrastructure and a brownfield site that is already connected to an electric grid for pump power.

5.1 Model Validation

In order to verify that the model approximates reality, the Electratherm Green Machine was simulated under conditions similar to those of a test conducted at the University of Alaska Fairbanks. The simulated results were compared to the results of that Green Machine test. There were some difficulties in re-creating exact conditions because some values were not precisely recorded. For example, operating ranges for the high and low pressures of the working fluid were stated, but specific measurements were not included. Other values, were assumed while sizing the ORC for the test, but not measured after the installation because the report was interested in the performance of the whole unit rather than modeling it. These values include the heat transfer coefficients and areas of the heat exchangers, as well as the isentropic efficiencies of the pump and expander.

Despite the differences in these parameters between the model and the report, the model was still validated based on the general trends in the output power. Higher source fluid temperatures yield more power. Greater mass flow rates of the source and sink similarly provide a greater output power, though this is limited by the area and heat transfer coefficient parameters of the heat exchangers. These limits could be increased with a larger heat exchanger area or heat transfer coefficient. These patterns and trends follow what is expected for an ORC system.

5.2 Greenfield

The greenfield simulations demonstrated the expected increase of available power output during winter months. According to the model, even more power could be produced by increasing the mass flow rate of the working fluid. However, this assumes the isentropic efficiency of the turbine expander is equal in the two cases which is unlikely. The additional mass means the fluid does not fully vaporize which is not typical for ORC systems because the efficiency is not constant under all conditions.

While the available power gained by increasing the flow rate of the working fluid is limited by the vaporization, that flow rate limit could be increased by also increasing the flow rates of the source and sink fluids. Hypothetically, the higher flow rates mean larger pumps and heat exchangers must be used for the system, increasing the total cost, but that should be offset by the increase in output power. Realistically though, only so much hot water can be drawn from geothermal resources before the source temperature begins to drop. This can be alleviated by re-injecting the source effluent up to a point. However, the model assumes the resources are steady, and if the flow rates are increased too much that assumption would no longer be valid.

5.3 Brownfield

In the brownfield case study it was shown that the ORC could not produce enough electrical power to drive the district heating loop pumps from the inverter as a prime power source. However, there was sufficient mechanical power produced, but due to inefficiencies and parasitic loads there was insufficient net output electrical power remaining to serve the district heating loop pumps. This indicates there may be enough power from the local resource to operate the district heating system while the electrical grid is active and capable of regulating the frequency and voltage of the induction generator. However, the whole system would still go down during a power outage and the diesel generators would still need to be used to give the community heat, albeit with lower fuel consumption than without the ORC system.

One possible solution is to increase the size of the evaporator area. This would allow more heat to flow from the water to the working fluid, meaning more fluid could be moved while still fully vaporizing. Unfortunately, the cost of the system would go up as well due to the larger heat exchanger.

Another option could be to bypass electrical conversion entirely, eliminating several inefficiencies along the way. The simulated ORC produced more mechanical power than electrical, and the mechanical load to drive the pumps is actually less than the rated electrical load. A system could be developed to connect the ORC expander to a mechanical pump to drive the district heating loop. Depending on the design this could be done with a direct coupling or through a gearbox of some kind. Of course other inefficiencies would be introduced and controlling the flow would be challenging, but it might be worth further examination.

5.4 Future Work

One improvement that the model needs is a user friendly graphical interface. Currently, a MATLAB® script is run in order to initialize all the input variables and parameters, then the Simulink simulation is executed, and finally a second script is used to generate the plots. Combining some of these steps into a graphical user interface, this model could be more readily utilized by other researchers and potentially developed for commercial use. In addition to the interface, there are other potential improvements related to the transient, thermal, and electrical aspects of the model.

5.4.1 Transient Model

This model was designed to examine steady-state results. It looks at the energy balance of each component to simulate how they interact over the long term. This means it is unable to accurately capture transient dynamics after a change in load, temperature, or flow rate. Each of those fluctuations can occur at different time scales and affect the system dynamics differently. It is important to know the system is capable of providing primary power while maintaining grid frequency and voltage under those different perturbations.

5.4.2 Thermal Model

As described previously, the model is perfectly efficient at transferring the heat and none is lost to the ambient environment. In reality, fluid in the heat exchangers, pumps, expanders, and pipes will experience some amount of heat loss or gain to the surrounding area. Furthermore, the model only calculated pressure changes across the pump and expander, where as fluids in actual systems will see some pressure drops through each component. The overall accuracy of the model could be improved by accounting for these additional routes of heat flow and pressure changes.

Another implementation that could improve system performance is an optional pre-heater that several commercial systems already use. This optional heat exchanger is inserted in the loop between the pump and evaporator on the high pressure side effectively increasing the area of the evaporator. Sometimes the pre-heater uses a different heat source from the primary source. Even the heat of the working fluid coming off of the expander before flowing through the condenser could be used. This allows the system to recycle some of the heat that was not converted into mechanical energy letting it operate at a slightly higher efficiency, but at the expense of an additional component.

5.4.3 Electrical Model

The type of generators simulated as a part of this project only included squirrel cage induction machines because they are relatively inexpensive to build and maintain, and are therefore commonly used in commercial ORC systems. They are not, however, ubiquitous. It would be beneficial to include models of additional generator types such as DC or permanent magnet synchronous machines. This would allow the user to compare systems made by different manufacturers which use various generator technologies.

Energy storage is often an important piece of infrastructure in microgrids. Depending on the load characteristics, it may be necessary in a transient model where the load power temporarily exceeds the power produced by the ORC generator. Additionally, the storage could also help maintain the frequency or voltage stability of the microgrid, even if the available power is capable of meeting load demands.

5.5 Final Thoughts

Overall, this thesis demonstrated that for remote greenfield microgrids, modest loads can be primarily powered off of these low temperature geothermal ORC systems. For Pilgrim Hot Springs in Alaska, a small greenhouse could be designed and built to operate in the winter using LED grow lights. This could provide a source of fresh local vegetables to the nearby community of Nome throughout the year.

As for brownfield microgrids, there is less flexibility because the loads are already present and cannot be designed around the available source. Specifically, in the village of Bergstaðir, Iceland the geothermal ORC prime power system presented here could not on its own fully supply the electrical power required for pumps in the existing district heating system. The ORC could, however, provide most of the necessary power meaning that a significant portion of the diesel fuel used to operate the district heating system during power outages could be displaced.

With greater utilization of locally available resources reliance on fossil fuels could be reduced. A number of remote areas rely on diesel fuel but have access to low temperature geothermal hot springs. The model developed for this thesis can be used to analyze more of these geothermal sites under consideration for both prime (grid-forming) and grid-supporting electric power production. Furthermore, by implementing some of the improvements to the model described above the analysis could be even more insightful and potentially result in improvements to the design of ORC systems for converting heat into mechanical and electrical power.

Bibliography

[1] G. Holdmann, D. Benoit, R. Daanen, A. Prakash, and C. Haselwimmer, "Pilgrim Hot Springs Geothermal System Conceptual Model," tech. rep., University of Alaska Fairbanks, Fairbanks, Alaska, 2013.

[2] G. Holdmann, "The Chena hot springs 400 kW Geothermal Power Plant: experience gained during the first year of operation, in: Chena Geothermal Power Plant Report," tech. rep., Chena Power LLC, Fairbanks, Alaska, 2007.

[3] "Alaska Railbelt Cooperative Transmission & Electric Company." `http://arctec.coop/`. [Online; accessed 2016-05-09].

[4] T. P. Hughes, *Networks of Power: Electrification in Western Society, 1880-1930*. Johns Hopkins University Press, 1983.

[5] S. M. Schoenung and W. V. Hassenzahl, "Long- vs . Short-Term Energy Storage Technologies Analysis A Life-Cycle Cost Study A Study for the DOE Energy Storage Systems Program," tech. rep., Sandia National Laboratories, 2003.

[6] E. Ortjohann, W. Sinsukthavorn, M. Lingemann, N. Hamsic, M. Hoppe, P. Wirasanti, A. Schmelter, S. Jaloudi, and D. Morto, "Recycling Hierarchical Control Strategy of Conventional Grids for Decentralized Power Supply Systems," in *Energy Efficiency - A Bridge to Low Carbon Economy*, InTech, Mar. 2012.

[7] A. Engler, "Control of parallel operating battery inverters," in *Photovoltaic Hybrid Power Systems Conference*, pp. 1–4, 2000.

[8] P. Strauss and A. Engler, "AC Coupled PV Hybrid Systems and Micro Grids - State of the Art and Future Trends," in *World Conference on Photovoltaic Energy Conversion*, (Osaka, Japan), pp. 2129–2134, 2003.

[9] T. Vandoorn, J. De Kooning, B. Meersman, and L. Vandevelde, "Review of primary control strategies for islanded microgrids with power-electronic interfaces," *Renewable and Sustainable Energy Reviews*, vol. 19, pp. 613–628, Mar. 2013.

[10] F. Katiraei, R. Iravani, N. Hatziargyriou, and A. Dimeas, "Microgrids management," *IEEE Power and Energy Magazine*, vol. 6, pp. 54–65, May 2008.

[11] M. Prodanović and T. Green, "High-Quality Power Generation Through Distributed Control of a Power Park Microgrid," *IEEE Transactions on Industrial Electronics*, vol. 53, pp. 1471–1482, Oct. 2006.

[12] J.-F. Chen and C.-L. Chu, "Combination voltage-controlled and current-controlled PWM inverters for UPS parallel operation," *IEEE Transactions on Power Electronics*, vol. 10, no. 5, pp. 547–558, 1995.

[13] K. Siri, C. Lee, and T.-E. Wu, "Current distribution control for parallel connected converters. I," *IEEE Transactions on Aerospace and Electronic Systems*, vol. 28, pp. 829–840, July 1992.

[14] Y. W. Li and C.-N. Kao, "An Accurate Power Control Strategy for Power-Electronics-Interfaced Distributed Generation Units Operating in a Low-Voltage Multibus Microgrid," *IEEE Transactions on Power Electronics*, vol. 24, pp. 2977–2988, Dec. 2009.

[15] M. Starke, L. M. Tolbert, and B. Ozpineci, "AC vs. DC distribution: A loss comparison," in *2008 IEEE/PES Transmission and Distribution Conference and Exposition*, pp. 1–7, IEEE, Apr. 2008.

[16] H. Pang, E. Lo, and B. Pong, "DC Electrical Distribution Systems in Buildings," in *2006 2nd International Conference on Power Electronics Systems and Applications*, pp. 115–119, IEEE, Nov. 2006.

[17] M. Grotzbach and C. Ried, "Investigation of AC/DC converter harmonics by an analytical based time-discrete approach," *IEEE Transactions on Power Delivery*, vol. 12, pp. 874–880, Apr. 1997.

[18] H. B. Estes, A. Kwasinski, R. E. Hebner, F. M. Uriarte, and A. L. Gatlozzi, "Open Series Fault Comparison in AC & DC Micro-grid Architectures," in *INTELEC, International Telecommunications Energy Conference*, 2011.

[19] H. Lotfi and A. Khodaei, "AC Versus DC Microgrid Planning," *IEEE Transactions on Smart Grid*, 2015.

[20] G. Nellis and S. Klein, *Heat Transfer*. Cambridge University Press, 2009.

[21] B. Norden, "Geothermal Energy Utilization in Low-Enthalpy Sedimentary Environments," tech. rep., Deutsches GeoForschungsZentrum (GFZ), Potsdom, Germany, 2011.

[22] J. Kreider, *Medium and High Temperature Solar Processes*. Academic Press, 1979.

[23] S. J. Chapman, *Electric Machinery Fundamentals*. McGraw Hill, 5th ed., 2005.

[24] L. Ouazenne and G. McPherson, "Analysis of the Isolated Induction Generator," *IEEE Power Engineering Review*, vol. PER-3, pp. 59–59, Aug. 1983.

[25] N. Ammasaigounden, M. Subbiah, and M. Krishnamurthy, "Wind-driven self-excited pole-changing induction generators," *IEE Proceedings B Electric Power Applications*, vol. 133, no. 5, p. 315, 1986.

[26] R. Bansal, "Three-Phase Self-Excited Induction Generators: An Overview," *IEEE Transactions on Energy Conversion*, vol. 20, pp. 292–299, June 2005.

[27] S. Müller, M. Deicke, and R. De Doncker, "Doubly fed induction generator systems for wind turbines," *IEEE Industry Applications Magazine*, vol. 8, no. 3, pp. 26–33, 2002.

[28] E. Bogalecka, "Dynamics of the power control of a double fed induction generator connected to the soft power grid," in *ISIE '93 - Budapest: IEEE International Symposium on Industrial Electronics Conference Proceedings*, pp. 509–513, IEEE, 2002.

[29] N. Mohan, T. Undeland, and W. Robbins, *Power Electronics Converters, Applications, and Design.* Wiley, 3rd ed., 2003.

[30] A. Mohd, E. Ortjohann, W. Sinsukthavorn, M. Lingemann, N. Hamsic, D. Morton, and D. Road, "Supervisory Control and Energy Management of an Inverter-based Modular Smart Grid," in *IEEE/PES Power Systems Conference and Exposition*, pp. 2–7, 2009.

[31] A. Alolah, "Static power conversion from three-phase self-excited induction and reluctance generators," *Electric Power Systems Research*, vol. 31, no. 2, pp. 111 – 118, 1994.

[32] S.-H. Song, S.-i. Kang, and N.-k. Hahm, "Implementation and control of grid connected AC-DC-AC power converter for variable speed wind energy conversion system," in *Eighteenth Annual IEEE Applied Power Electronics Conference and Exposition, 2003. APEC '03.*, pp. 154–158, IEEE, 2003.

[33] H. Okada, T. Ezaki, K. Ogawa, H. Koba, M. Takeo, K. Funaki, S. Sato, F. Irie, J. Chikaba, K. Terazono, M. Takamatsu, M. Kawakami, and M. Hirano, "Experimental study of SMES system with DC intertie for power line stabilization," in *PESC '88 Record., 19th Annual IEEE Power Electronics Specialists Conference*, pp. 326–333, IEEE, 1988.

[34] I. H. Bell, J. Wronski, S. Quoilin, and V. Lemort, "Pure and pseudo-pure fluid thermophysical property evaluation and the open-source thermophysical property library coolprop," *Industrial & Engineering Chemistry Research*, vol. 53, no. 6, pp. 2498–2508, 2014.

[35] A. Pezzuolo, A. Benato, A. Stoppato, and A. Mirandola, "The ORC-PD: A versatile tool for fluid selection and Organic Rankine Cycle unit design," *Energy*, vol. 102, pp. 605–620, May 2016.

[36] L. Pierobon, A. Benato, E. Scolari, F. Haglind, and A. Stoppato, "Waste heat recovery technologies for offshore platforms," *Applied Energy*, vol. 136, pp. 228–241, Dec. 2014.

[37] G. Besagni, R. Mereu, G. Di Leo, and F. Inzoli, "A study of working fluids for heat driven ejector refrigeration using lumped parameter models," *International Journal of Refrigeration*, vol. 58, pp. 154–171, Oct. 2015.

[38] S. Quoilin, I. Bell, A. Desideri, P. Dewallef, and V. Lemort, "Methods to Increase the Robustness of Finite-Volume Flow Models in Thermodynamic Systems," *Energies*, vol. 7, pp. 1621–1640, Mar. 2014.

[39] H. M. Nilsen, K.-A. Lie, and O. Andersen, "Robust simulation of sharp-interface models for fast estimation of CO2 trapping capacity in large-scale aquifer systems," *Computational Geosciences*, vol. 20, pp. 93–113, Feb. 2016.

[40] F. P. Incropera, D. P. DeWitt, T. L. Bergman, and A. S. Lavine, *Fundamentals of Heat and Mass Transfer*. Wiley, 3rd ed., 1990.

[41] J. Pyrhonen, T. Jokinen, and V. Hrabovcova, *Design of Rotating Electrical Machines*. Wiley, 2013.

[42] J. E. Vrancik, "Prediction of Windage Power Loss in Alternators," Tech. Rep. October, National Aeronautics and Space Administration Lewis Research Center, Cleveland, OH, 1968.

[43] C.-s. Lin, D. Huang, G. Holdmann, V. Avadhanula, D. Light, T. Johnson, R. Coen, and D. Pelunis-Messier, "Green Machine Organic Rankine Cycle Field Test Project," tech. rep., Alaska Center for Energy and Power, Fairbanks, Alaska, 2014.

[44] Chemical Engineer's Guide, "Pump Sizing Calculator," 2017.

[45] J. F. Batir, D. D. Blackwell, and M. C. Richards, "Updated Surface Heat Flow Map of Alaska," *Geothermal Resources Council Transactions*, vol. 37, pp. 927–932, 2013.

[46] C. Haselwimmer, A. Prakash, and G. Holdmann, "Quantifying the heat flux and outflow rate of hot springs using airborne thermal imagery: Case study from Pilgrim Hot Springs, Alaska," *Remote Sensing of Environment*, vol. 136, pp. 37–46, Sept. 2013.

[47] Alaska Center for Energy and Power, "Pilgrim Hot Springs Geothermal Exploration, 2010-2014, Final Report," tech. rep., University of Alaska Fairbanks, 2014.

[48] G. Tamulaitis, P. Duchovskis, Z. Bliznikas, K. Breive, R. Ulinskaite, A. Brazaityte, A. Novičkovas, and A. Žukauskas, "High-power light-emitting diode based facility for plant cultivation," *Journal of Physics D: Applied Physics*, vol. 38, pp. 3182–3187, Sept. 2005.

[49] A. S. Loftsdottir and R. I. Thorarinsdottir, *Energy in Iceland Historical Perspective, Present status, Future outlook.* 2nd ed., 2006.

Appendix A

List of ORC Manufacturers

A partial list of ORC system developers can be seen in Table A.1 with fewer than ten documented installed systems. A list of commercial systems with more than ten documented systems installed can be seen in Table A.2. Both tables also include, if available, the working fluid used, the mechanical drive, the approximate maximum rotational speed, the generator type, and the rated output. These tables show R245-fa[1] is commonly used as a working fluid among these manufacturers. Furthermore, these devices mostly use induction machines or PMSGs, although there is a documented instance using a DC generator. For the machines using PMSGs, a grid-following electronic conversion device is used to convert the generator output to match that of the grid, while the induction generators connect directly to the grid for a source of reactive power and to regulate their frequency and voltage.

---

[1] $CF_3CH_2CHF_2$ (1,1,1,3,3- pentafluoropropane)

Table A.1. Manufacturers and developers of ORCs with fewer than ten documented installed systems. Also listed are the working fluids, mechanical drives, rated operating speeds, generator types, and rated outputs.

Company	**Working Fluid**	**Mech. Drive**	**Rated RPM**	**Gen. Type**	**Size (kW)**
Air Squared		Scroll	2600		12
Termo2Power	R245-fa	Rotary Lobe			10 to 300
Climeon		Turbine			150
Calnetix/ Access Energy	R245-fa	Turbine	30000	PMSG	120
Verdicorp		Turbine	45000	PMSG	65 to 380
Inifinity Turbine	R245-fa, supercrit. CO_2	Radial Outflow Turbine	3600	Induction & DC	10 and 50
Ener-G-Rotors		Trochoidal Gear Engine using ge-rotor			40 and 60
Phoenix	R245-fa, Novec-649, Cyclohexane				25, 50, 100 and 250

Table A.2. Manufacturers and developers of commercial ORCs with more than ten documented installed systems. Also listed are the working fluids, mechanical drives, rated operating speeds, generator types, and rated outputs.

Company	**Working Fluid**	**Mech. Drive**	**Rated RPM**	**Gen. Type**	**Size (kW)**
Electratherm	R245-fa	Twin Screw	5000	Induction	35, 65 and 110
E-Rationale	R245-fa, SES36	Single Screw Radial Inflow	3600	Induction	55, 75, 110 and 132
Exergy		Radial Outflow Turbine			125 and up
Zuccato	Hydrofluorocarbon mixture	Radial Inflow Turbine	18000	PMSG	30, 40 and 50
Enogia	R245-fa	Turbine			10, 20, 40 and 100
Clean Energy Technologies	R245-fa	Turbine	27500		125
Tri-O-Gen		Turbine			165